Chapter 7

High-Resolution X-Ray Diffraction of III–V Semiconductor Thin Films

Hédi Fitouri, Mohamed Mourad Habchi and Ahmed Rebey

Additional information is available at the end of the chapter

http://dx.doi.org/10.5772/65404

Abstract

In this chapter, we will address the structural characterization of III–V semiconductor thin films by means of HRXRD. We first give an overview on the basic experimental apparatus and theory element of this method. Subsequently, we treat several examples in order to determine the effect of doping, composition and strain on structural properties of crystal. Analysed layers were grown by metal organic vapour phase epitaxy (MOVPE). Films treated as examples are selected in order to bring the utility of characterization technique. Here, we investigate GaAs/GaAs(001), GaAs:C/GaAs(001), GaN/Si(111), GaN:Si/Al_2O_3(001), GaAsBi/GaAs(001) and InGaAs/GaAs(001) heterostructures by using different scans for studying numerous structural layers and substrate parameters. Different scan geometries, such as ω-scan, $\omega/2\theta$-scan and map cartography, are manipulated to determine tilt, deformation and dislocation density induced by mismatch between layer and substrate. This mismatch is originated from the difference between the chemical properties of two materials generated by doping or alloying. Such HRXRD measurements are explored through the angular spacing between peaks of the substrate and layer. The half of full width maximum (HFWM) of peak layer intensity is a crucial qualitative parameter giving information on defect density in the layer.

Keywords: HRXRD, thin films, III–V semiconductors, alloys, stress, reciprocal map

1. Introduction

Over the past decade, the epitaxy of structures based on III–V materials has emerge to become of vital commercial importance within the electronics, optoelectronics and telecommunication industries. With rapid developments of epitaxy apparatus (such as molecular beam epitaxy or metal organic chemical vapour epitaxy) and *in situ* diagnostics (such as RHEED and

reflectometry), the elaborated active part of heterostructure has now come in the vicinity of idealism. However, such deviation from ideal properties (structural, optical or electrical) can reduce the device response. In this way and for economical reasons, it is desirable to characterize the as-grown layers prior to further processing. Indeed, high-resolution of X-ray diffraction (HRXRD) is now one of the widely used tools for non-invasive determination of the composition, thickness and perfection of the epitaxial layers of compound semiconductors. Recently, there had been great interest in the use of this technique with different scan geometries.

In this chapter, we will address the structural characterization of III–V semiconductor thin films by means of HRXRD. We first give an overview on the basic experimental apparatus of this method. Subsequently, we treat several examples in order to determine the effect of doping, composition and strain on structural properties of crystal.

2. Experimental details and theory element

All layers investigated in this work are elaborated by metal organic vapour phase epitaxy (MOVPE) technique [1–8].

For arsenide layers, we use a Bruker D8 diffractometer. An X-ray tube with a copper cathode generates the incident beam (1.54056 Å). In order to obtain highly monochromatic incident beam, we use a monochromator constituted by four Ge(022) crystals which gave a resolution of $\frac{\Delta\lambda}{\lambda} < 1.5\times10^{-4}$. The scattered beam can be detected by a scintillation point detector as reported in the left of **Figure 1**. The layer, that shall be examined, is mounted on the sample holder. As shown in the right of **Figure 1**, we denote ω as the angle between X-ray beam and the crystal surface, 2θ, the detector position, φ, the rotation angle around the normal of crystal and τ (or χ), the inclination angle of crystal in a perpendicular plane to the surface. This configuration gives a coupled and uncoupled scans, such as ω-scan (or rocking curve scan) and $\omega/2\theta$ scan.

For nitride layer, HRXRD measurements have been performed with a Bede 200 diffractometer equipped with a four-crystal monochromator in Si[220] mode.

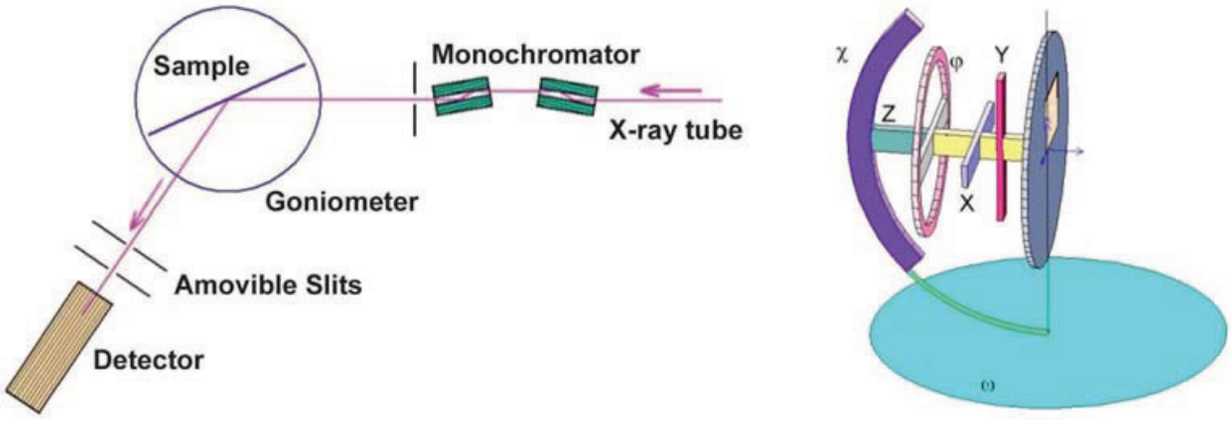

Figure 1. In the left, optical path of X-ray beam for the used goniometer. In the right, goniometer axes.

http://dx.doi.org/10.5772/65404

The simple form of Bragg equation for the lattice planes with Miller indices (*hkl*) and the distance d_{hkl} between two such adjacent planes is given by

$$2d_{hkl}\sin\theta = n\lambda \tag{1}$$

where:

- For cubic lattice with lattice constant a,$d_{hkl} = \frac{a}{\sqrt{h^2+k^2+l^2}}$,
- For hexagonal lattice with lattice constant a and c, $d_{hkl} = \frac{a}{\sqrt{\frac{4}{3}(h^2+k^2+hk)+(\frac{a}{c})l^2}}$.

Differentiation of Bragg equation and subsequent division of the result by the same equation yields the differential Bragg equation

$$\frac{\Delta d_{hkl}}{d_{hkl}} + \Delta\theta.\cot(\theta) = \frac{\Delta\lambda}{\lambda} \tag{2}$$

In our case, the spectral width of the incident beam is neglected ($\frac{\Delta\lambda}{\lambda}\sim 0$).

3. Application for thin films

3.1. Bulk films and substrates

Bulk substrates are characterized by a perfect crystallographic structure with an insignificant defect density. In HRXRD measurements, they have been used as a reference for Bragg angular measurements. But it is vital to minimize intrinsic and extrinsic effects, such as tilt substrate or tilt substrate-to-holder sample (due to inaccurate sample mounting).

As an example, in order to determine the disorientation of GaAs substrate, the (004) rocking curves peak angles (ω_S) were taken for some azimuthal angle φ as shown in **Figure 2**. As mentioned earlier, ω_S variation follows the relation: $\omega_s(004) = \langle\omega_s\rangle + A\cos(\varphi - \varphi_0)$.

where A is the tilt or the disorientation to the absolute crystallographic substrate orientation.

Similarly, $\chi(004) = \langle\chi\rangle + A\sin(\varphi - \varphi_0)$ or $\chi(004) = \langle\chi\rangle - A\sin(\varphi - \varphi_0)$.

The best fit of experimental data by expression reported below allows the values of $\langle\omega_s\rangle = 33.0308^\circ$ and $A = 0.472^\circ$. By using Bragg's law, we can measure the lattice parameter of GaAs substrate $a_s = \frac{2\lambda_{CuKa1}}{\sin\langle\omega_s\rangle} = 5.6526\mathring{A}$. The manufacturer indicates that this commercial substrate is exactly orientated to (001) with a tolerance of ±0.5° and the lattice parameter is of $5.6533\mathring{A}$ corresponding to a Bragg angle of 33.028°. The difference between the two Bragg angles represents an error of about 0.003°. Also, the value of tilt A is in the same order of the tolerance given by the substrate producer.

3.2. Homoepitaxy

Homoepitaxy is the growth of a layer on the substrate where the two materials have the same physical characteristics (Si/Si, GaAs/GaAs, etc.). Such a structure is characterized by small full-

width at half-maxima (FWHMs) of measured peaks when growth is perfectly optimized and no supplementary information is given about the layer properties.

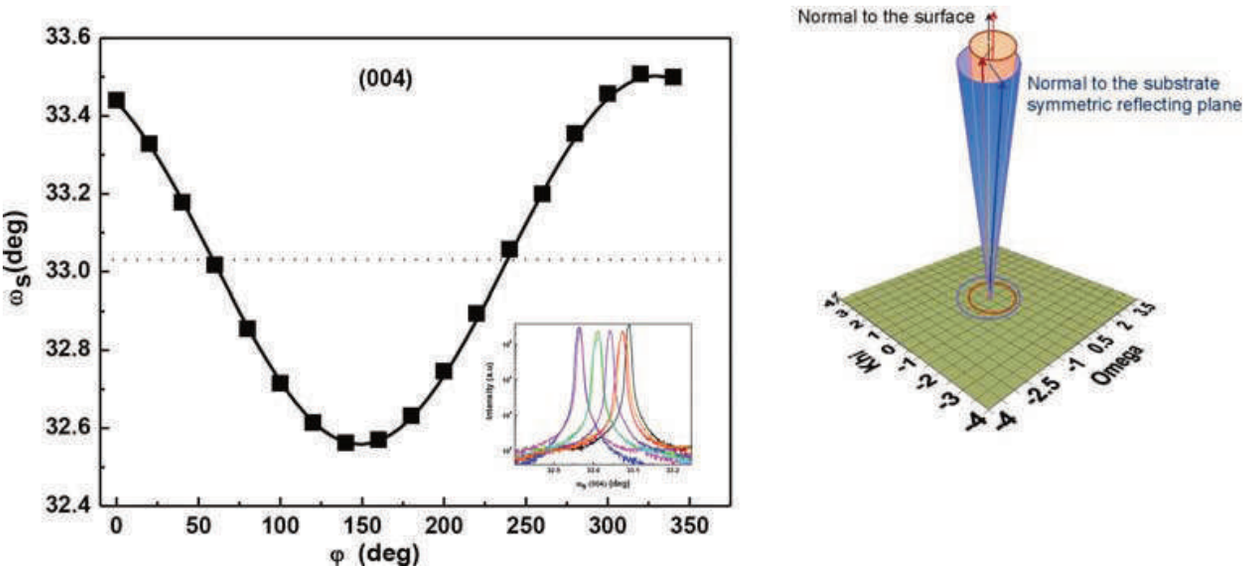

Figure 2. In the left, measured Bragg angle GaAs substrate of (004) rocking curves as a function of the azimuthal angle φ fitted by (the solid line) a sinusoidal equation. In the inset a series of rocking curves are shown. In the right, illustration of ω-scan around the normal to the substrate.

Doping of semiconductors is required to improve the electrical properties of material. In numerous applications, it is necessary to dope strongly n+ or p+ any part of the structure. Indeed, for tunnel effect or to obtain ohmic contact in GaAs, doping levels above 10^{19} cm^{-3} were needed. This requirement gives rise to a modification in structural properties of the doped layer. Yet, this deviation to ideal structure is clearly observed when atomic covalent radius of impurity is smaller or higher compared to atomic radius of matrix constituents. As an example, the doping of GaAs by carbon (C) gives rise to tetragonal distortion of GaAs caused by smaller covalent radius of C (r_c = 0.77 Å) compared to those of gallium (r_{Ga} = 1.26 Å) and arsenic (r_{As} = 1.20 Å). HRXRD is sensitive to this smaller deviation and will be used to determine the doping concentration.

The perpendicular lattice mismatch of C-doped GaAs was investigated by measuring (004) reflection and according to the following relation:

$$\varepsilon^{\perp} = \left(\frac{\Delta a}{a}\right)^{\perp} = -\Delta\theta_B \cot(\theta_B) \tag{3}$$

where $\theta_B = 33.028^\circ$ is the Bragg angle for (004) reflection.

On the other hand, in order to investigate the conditions of strain relaxation we have measured the parallel lattice mismatch $\Delta a_{//}$. Indeed, to find the in-plane lattice mismatch, an asymmetric (±1, ±1, ±5) reflection should be determined. The inclination angle φ is between a reflection from a lattice plane and the surface. The measurement of a reflection can be carried out at high

http://dx.doi.org/10.5772/65404

angle $\theta_B + \varphi$ or at a low angle $\theta_B - \varphi$. We can calculate the components of lattice mismatch from the measured differences in Bragg angle and lattice-plane orientation with regard to the substrate according to [9]:

$$\varepsilon^{\perp} = \frac{\Delta a^{\perp}}{a_{GaAs}} = \Delta\varphi tg\varphi - \Delta\theta \cot\theta_B \tag{4}$$

$$\varepsilon^{//} = \frac{\Delta a^{//}}{a_{GaAs}} = -\Delta\varphi \cot\varphi - \Delta\theta \cot\theta_B \tag{5}$$

In our case $\theta_B = 45.064°$ and $\varphi = 15.791°$.

For more details, let $\Delta\omega_a$ be the angular spacing between peaks of the substrate and of C-doped GaAs layer in $\omega/2\theta$ curve, and $\Delta\omega_b$ the same quantity measured after rotating the crystal by 180° around the normal to the wafer surface. Then, for (115) reflection

$$\Delta\varphi = \frac{1}{2}(\Delta\omega_a - \Delta\omega_b), \tag{6}$$

$$\Delta\theta_B = \frac{1}{2}(\Delta\omega_a + \Delta\omega_b). \tag{7}$$

The double determination of $\varepsilon^{\perp}$ from (004) and (115) reflections gives a more precision on its values than that of $\varepsilon^{//}$.

Based on this result, it is possible to determine the compensation ratio θ of our films using the Vegard's law in the strained form [10, 11].

$$\left(\frac{\Delta a^{\perp}}{a_{GaAs}}\right)_{strained} = \left(\frac{1+\upsilon}{1-\upsilon}\right)\left(\frac{\Delta a\perp}{a_{GaAs}}\right)_{relaxed} = 1.9\left(\frac{\Delta a\perp}{a_{GaAs}}\right)_{relaxed}. \tag{8}$$

We assume that the substituted carbon in the gallium site (C_{Ga} usually used to estimate the compensation) is the dominant cause of the compensation described by [12, 13]

$$\left(\frac{\Delta a^{\perp}}{a_{GaAs}}\right)_{relaxed} = \frac{4}{\sqrt{3}a_{GaAs}N}(\Delta r_{As} + \Theta\Delta r_{Ga})\frac{p_H}{(1-\Theta)} \tag{9}$$

where Δr_{As}= -0.43 Å and Δr_{Ga}= -0.49 Å are the difference between the covalent radii of C and As and Ga, respectively. $N = 2.22 \times 10^{22}$ cm^{-3} is the number of gallium or arsenic atoms per cm^3 in pure GaAs crystal and $\upsilon = 0.31$ is the Poisson's ratio.

Figure 3 illustrates a comparison between experimental data results and curves calculated for strained or relaxed states and with different compensation ratios. Using this dependence between $\frac{\Delta a^{\perp}}{a_{GaAs}}$ and p_H, we extrapolate the compensation ratio for any layer. We remark that the values deduced, using this consideration, are in the same order than that deduced by Hall Effect or SIMS measurements.

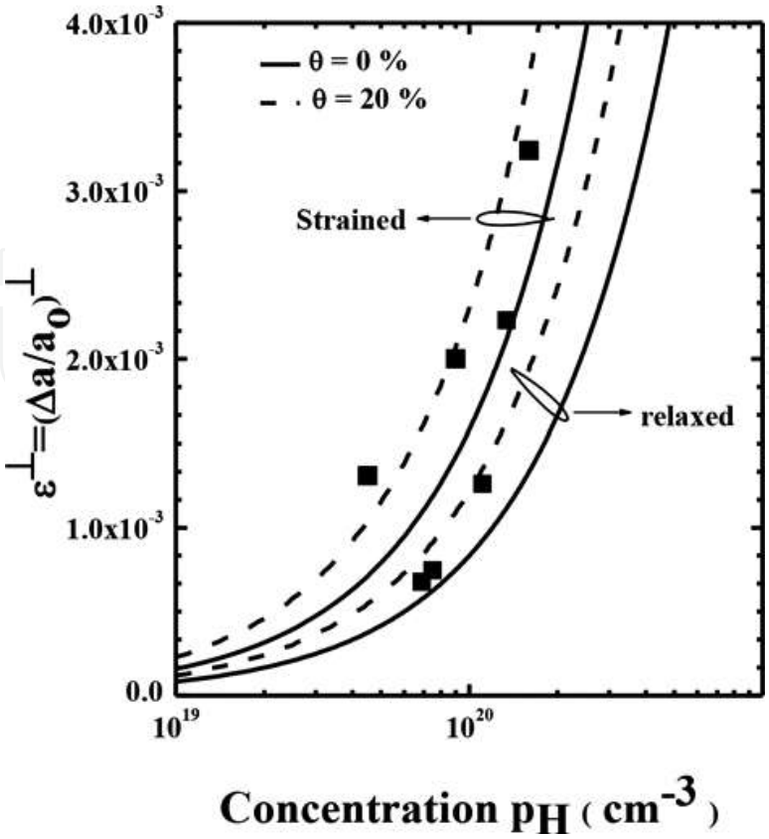

Figure 3. Perpendicular lattice mismatch ($\varepsilon^{\perp}$) of GaAs:C epilayers on GaAs substrates as a function of hole concentration p_H. The lines represent the predicted contraction based on Vegard's law for two values of compensation ratios $\theta = 0$ and $\theta = 0.25$.

3.3. Heteroepitaxy

Heteroepitaxy is the growth of a layer on the substrate where the two materials have different physical characteristics such as GaAs/Si, GaAs/Ge, GaN/Al_2O_3, etc. This means that the underlying substrate and the epitaxial layer are different materials with typically different lattice constants and perhaps even different crystal symmetry. Generally, this structure is characterized by misfit mismatch which generates stress and structural defects. In order to be accommodating to the substrate, the layer stays at less energetic equilibrium state which gives rise to appearance of tilt, twist and curvature of the system {layer + substrate}. HRXRD technique is able to determine these parameters.

3.3.1. Undoped GaN

III-Nitrides and related alloys cover a wide wavelength domain ranging from the red to the ultraviolet. Their interesting properties such as large and direct band gap make them attractive for the development of optoelectronic devices as well as high temperature and high power electronic applications. The MOVE growth of these materials is completed by using various substrates. However, the lack of suitable lattice matched substrate constitutes the major obstacle for further improvement in GaN material properties. Several attempts have been achieved for GaN growth on silicon substrate. Indeed, this choice is motivated by the availability with

low cost, the large size and high electrical and thermal conductivities of silicon. But, the success of GaN layer epitaxy requires a special growth procedure by using different processes (buffer layer, SiN treatment, etc.) in order to reduce the damage effects.

In this section, we focus on GaN layer grown on silicon substrate Si(111) where mismatch is of about 17%. This difference leads to the formation of a large number of defects (dislocations, cracks, etc.) and gives rise to layer mosaicity.

The GaN mosaicity can be usually described by two components of the misorientation: one is the tilt of *c*-axis with respect to the growth direction and the other is the twist of the columns orientation about the *c*-axis. GaN (00.l) ω-scans reflect the mosaic structure of the tilt among the crystallites. GaN (h0.l) ω-scans reflect the mosaic structure of twist between the crystallites. For symmetric (00.l) reflections, the full-width at half-maximum (FWHM) of the X-ray rocking curve (XRC) which characterize the tilt, was found to be around 1800 arcs. Note that both tilt and twist mosaics contribute to the rocking curve width of asymmetric (h0.l) reflections. For twist measurement, it is necessary to measure a series of reflections and extrapolate to an inclination angle χ of 90°. The plot of FWHM versus sin (χ) gives rise to an average twist of about 1.9° (**Figure 4**). The average twist was determined as half FWHM extrapolated to sin (χ) = 1. This high value of the twist can be explained by the interaction between hillocks of GaN during the nucleation process or dislocations which lead to a broad rocking curve width of GaN reflections.

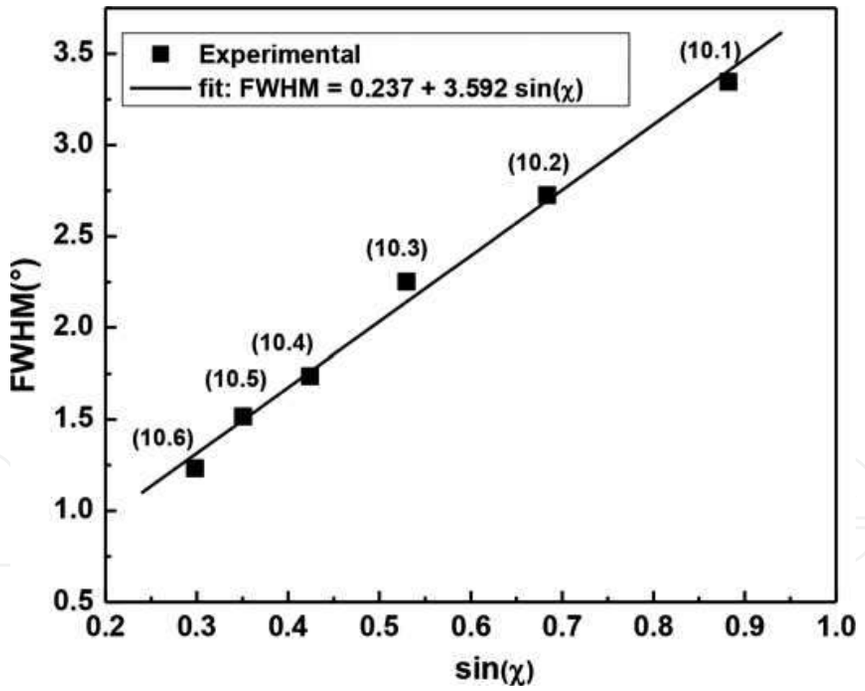

Figure 4. Evolution of FWHM (h0.l) plane reflections as a function of inclinations (χ) referring to (00.l) plane. The solid line represents the best linear fit of experimental data.

3.3.2. Si doped GaN

In order to study the effect of Si-doping on stress in GaN layers, HRXRD and Raman spectra measurements were carried out. **Figure 5** shows HRXRD patterns measured in $\theta/2\theta$ scan mode.

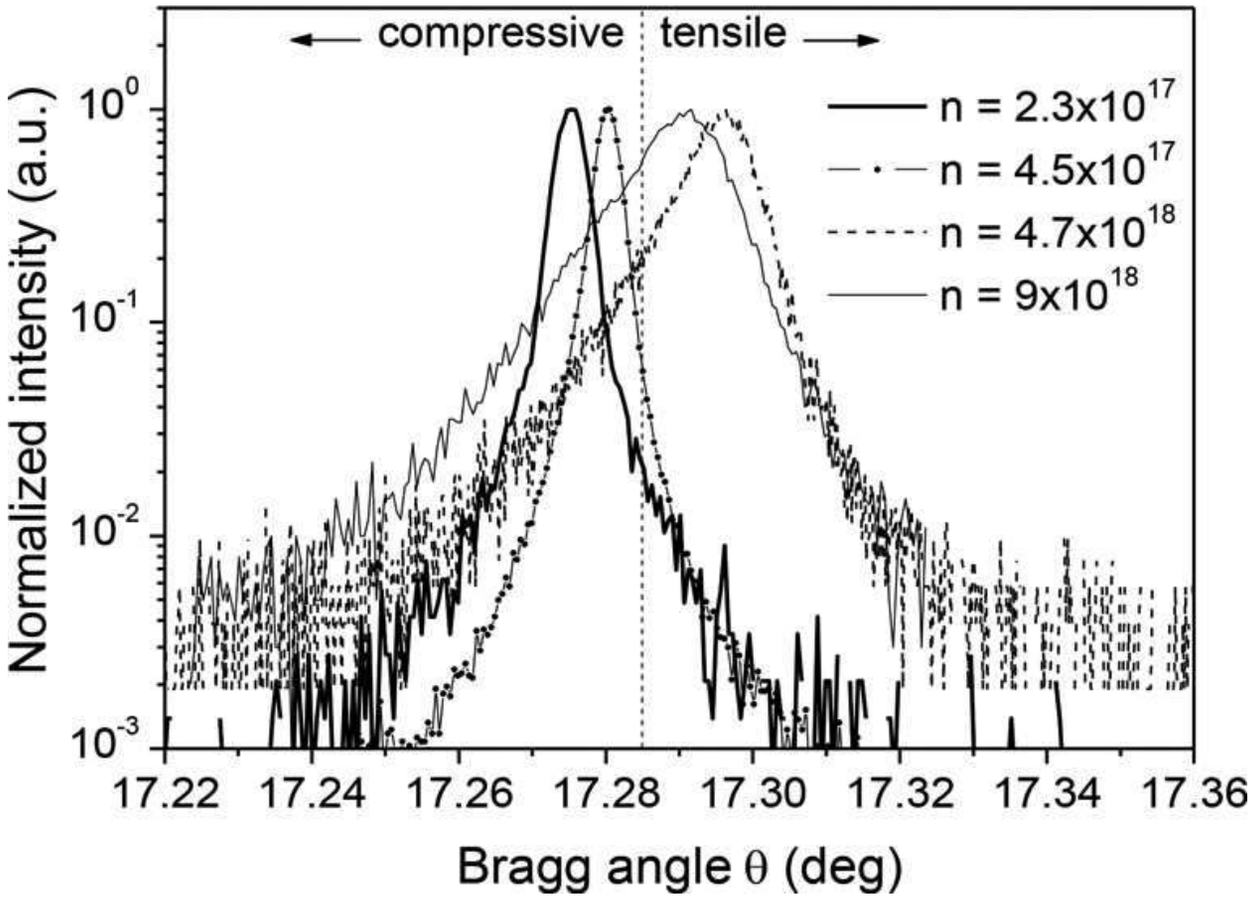

Figure 5. ω -scans of the Si-doped GaN samples.

The θ position shifts to the higher angle corresponding to smaller c lattice constant when Si concentration increases. The asymmetric shape of the ω-scan for high doping levels can be attributed to a stress gradient normal to the sample surface [14]. The in-plane stress $\sigma_{//}$ can be roughly determined from the relationships [15].

$$\sigma_{//} = \frac{a-a_0}{a_0}\left(C_{11} + C_{12} - 2\frac{C_{13}^2}{C_{33}}\right), \tag{10}$$

where C_{ij} are the elastic constants of GaN (C_{11} = 390 GPa, C_{12} = 145 GPa, C_{13} = 106 GPa, C_{33} = 398 GPa) [16]. a_0 is the lattice constant for strain-free bulk GaN (a_0 = 3.189 Å). The values of the a lattice parameter, measured by HRXRD, and the corresponding stress values $\sigma_{//}$ show that the incorporation of silicon not only leads to stress relaxation in GaN layers, but also induces tensile stress ($\sigma_{//} > 0$) for doping levels higher than 1.6×10^{18} cm^{-3}. According to our PL data analysis (not shown here), we attribute the strong band gap reduction in the Si-doped GaN layers is essentially due to the relaxation of stress in these layers.

The effect of silicon doping on the mechanism of stress relaxation and defect formation in GaN is still under discussion. One plausible explanation is that the relaxation increases with Si-induced defects formed during the cool-down process [17, 18]. Thus, we can assume that the incorporation of silicon leads to increase of the dislocation density in the GaN epilayer. Note that the dislocation densities in GaN-based materials have been generally measured by

transmission electron microscopy (TEM) and etch pit densities (EPDs). However, as non-destructive method, X-ray rocking curves (ω-scans) can be used to measure the dislocation densities with accuracy equal to TEM and EPDs. The theory elements of this technique are described by Gay et al. [19] and Hordon and Averbach [20], for the case of highly dislocated metal crystals and extended by Ayers [21] to the case of zinc-blende semiconductors.

The model developed by Ayers uses the rocking curve line width broadening owing to threading dislocations for calculation of their densities. Then, the square of the measured rocking curve line width β_m for the (*hkl*) reflection can be written as [21]:

$$\beta_m^2(hkl) = K_\alpha + K_\varepsilon \tan^2\theta \tag{11}$$

where $K_\alpha = 2\pi\ln(2b^2D)$, $K_\varepsilon = 0.09\, b^2D \mid \ln(210^{-7}cm\sqrt{D}|$, b is the length of the burgers vector and D is the dislocation density. K_α is the rocking curve broadening owing to angular rotation at dislocations. K_ε is the broadening produced by strain surrounding dislocations.

The plot of β_m^2 versus $\tan^2\theta$ should give rise to a straight line. The dislocation densities can be independently calculated from the slope (K_ε) as well as the intercept (K_α). The obtained results based on the two ways should be identical. A plot according to last equation for various X-ray peaks is shown in **Figure 6**. As predicted by the model, the symmetric and asymmetric reflections are on a single straight line. Dislocation densities calculated according the Ayers model from the slopes and intercepts of these linear fits are shown in **Figure 7**.

AFM data corresponding to the densities of surface depressions and pinned steps are also given for comparison. It is well known that the surfaces of GaN layers grown by MOVPE are typically dominated by these two kinds of dislocation mediated surface structures [22]. So, as seen in **Figure 7**, the dislocation densities calculated from the slopes (D_ε = 8.4 × 10^8 to 7.1 × 10^9 cm^{-2}) are in same order of magnitude with that obtained by AFM measurements (D_{AFM}=1.3 × 10^9 to 8 × 10^9 cm^{-2}). The lack of internal consistency (D_ε slightly different from D_α) may be explained by the existence of sources of rocking curve broadening other than dislocations that give rise to different relative amounts of rotational and strain broadening [21].

3.4. Alloys

The III–V materials have raised a fundamental attention in the field of optoelectronics and rapid electronics. Particularly, the alloy semiconductors have an exceptional amount of interests owing to the possible adjustment of band gap and lattice parameter by changing chemical composition. Recently, the technological progress of elaboration and process techniques provides a great opportunity to design new structure architecture and quantum nanostructure based on non-conventional semiconductor materials. This fact requires a suitability of characterization tools adapted to this advance.

3.4.1. GaAsBi alloy as a new material

Owing to the large size and core electronic structure of Bi atom, Bi-containing semiconductor alloy materials exhibit a small or negative band gap. The interesting properties of III–V-Bi alloy offer a great opportunity for possible design in optoelectronic application devices. Recent

results from various groups demonstrated that $GaAs_{1-x}Bi_x$ thin films can be produced by molecular beam epitaxy (MBE) [23–25] or by MOVPE [1, 2, 26–28]. Further, $GaAs_{1-x}Bi_x$ alloy presents temperature insensitivity of band gap required in the resolution of problems of the lasing wavelength fluctuations. The quality of epitaxial compound film is governed by thickness uniformity, degree of alloying and substrate temperature. Precisely, the growth behaviour of $GaAs_{1-x}Bi_x$ was quite different from that of usual ternary semiconductor alloys such as GaInAs and AlGaAs. A very narrow growth conditions are reported by comparison between structural and optical characterizations. In this way, HRXRD is comely tool to investigate the structural properties of this material.

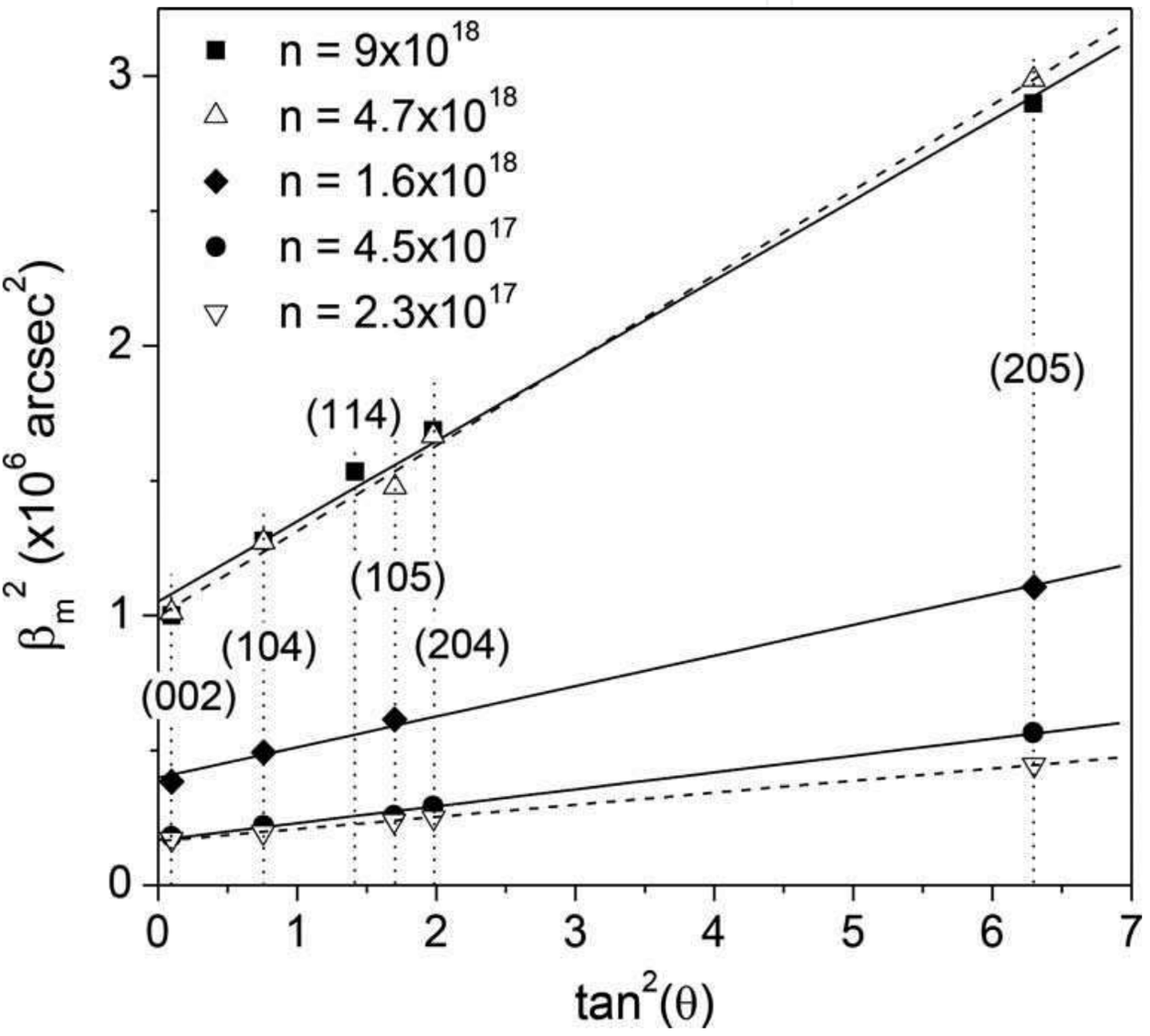

Figure 6. Square of rocking curve line width β_m (*hkl*) versus $\tan^2\theta$ for Si-doped GaN samples.

Figure 8 shows the diffraction pattern in the θ –2θ scan of X-ray diffraction measurement for a $GaAs_{1-x}Bi_x$ layer grown on p-type GaAs substrate. The spectrum shows three resolved peaks located at 31.627, 66.048 and 65.528° which are associated with the plane diffraction of (002)

http://dx.doi.org/10.5772/65404

and (004) GaAs and (004) $GaAs_{1-x}Bi_x$, respectively (detail is shown in the inset figure). No other phases were identified.

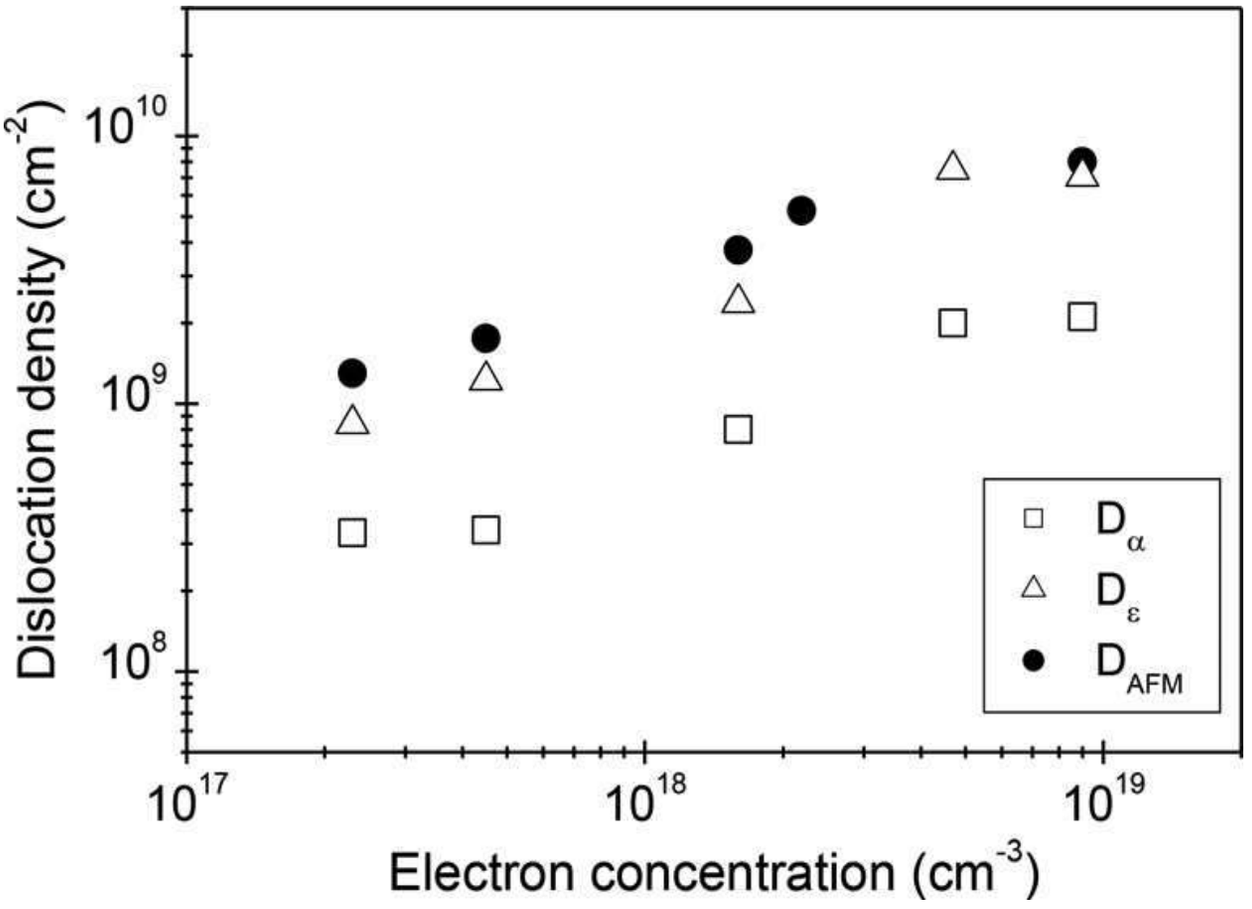

Figure 7. Dislocation densities calculated according to Ayers model from slopes (D_ε) and intercepts (D_α). AFM data are given for comparison.

HRXRD measurements of symmetric (004) and asymmetric (115) plane diffractions were carried out in order to determine the lattice parameter of $GaAs_{1-x}Bi_x$ and then Bi composition, as shown in **Figure 9**. In fact, the presence of two peaks relative to the layer and substrate diffractions, Pendellösung oscillations, seen in the wings of peaks, reveals a smooth and coherent interface. From these oscillations, we can calculate the layer thickness from Bragg's law: $t = \frac{\lambda \gamma_H}{\Delta\omega \sin(2\theta_B)}$. The period ($\Delta\omega$) is independent of scattering power of layer composition. $2\theta_B$ is the scattering angle, λ is the wavelength of the X-ray radiation and $\gamma_H = \sin(\theta_B + \varphi)$. φ is the angle between the diffraction planes and the surface.

The lattice constants in growth direction ($a_\perp$) and in the plane ($a_{//}$) of $GaAs_{1-x}Bi_x$ layer were calculated from the peak separation ($\Delta\theta_B$) between GaAs and $GaAs_{1-x}Bi_x$. $a_\perp$ is deduced from the spacing of the layer (004) plane (d_{004}) in the form of $a_\perp = 4\ d_{004}$ using a symmetric reflection (004). From asymmetric reflection (115), $a_{//}$ is deduced from the spacing of the layer (115) plane (d_{115}), in the form of $a_{//} = \sqrt{2}\left[\frac{1}{d_{115}^2} - \frac{25}{a_\perp^2}\right]^{\left(-\frac{1}{2}\right)}$.

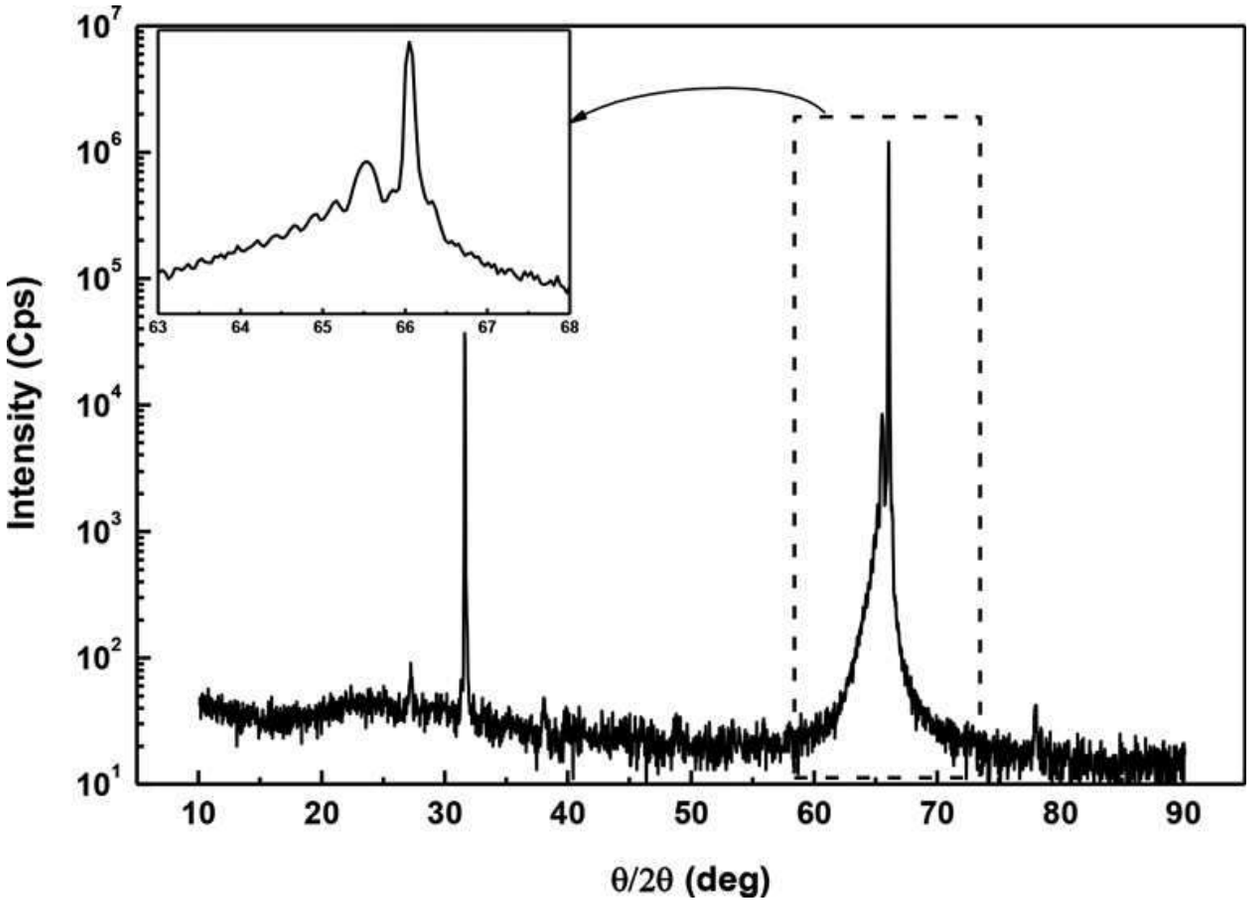

Figure 8. Diffraction pattern in the θ –2θ scan of X-ray diffraction measurement for a $GaAs_{1-x}Bi_x$ layer grown on (100) Zn doped GaAs substrate. The inset shows a zoom between $2\theta = 63^\circ$ and 68°.

The lattice constant (a_0) of unstrained cubic $GaAs_{1-x}Bi_x$ is assumed from

$$a_\perp = a_{//} + (a_0 - a_{//}) \frac{(C_{11} + 2C_{12})}{C_{11}} \tag{12}$$

where $C_{11} = 11.92$ and $C_{12} = 5.99$ are the elastic constants for $GaAs_{1-x}Bi_x$ which are supposed to be equal to those of GaAs. The Bi composition x, is calculated from a_0 using Vegard's law:

$$a_0 = x a_{GaBi} + (1-x) a_{GaAs} \tag{13}$$

where a_{GaBi} is the lattice constant of hypothetical zinc-blend GaBi and assumed to be 6.324 Å [29]. a_{GaAs}= 5.653 Å is the lattice constant of GaAs.

Thickness homogeneity and layer composition were characterized by recording (004) X-ray $\omega/2\theta$ curves for several positions in the layer surface. Small changes of 0.001 and 0.002° mm^{-1} have been detected for $\Delta\omega$ and $\Delta\theta_B$, respectively. Bi composition is estimated to 3.7% with a relative change of about 0.05% per mm. The layer thickness is about 50 nm. These values were also compared to those deduced from simulated X-ray patterns using the dynamical theory

http://dx.doi.org/10.5772/65404

shown as dotted lines in **Figure 9**. The tetragonal distortion induced by the epitaxy is taken into account using the elastic constants of GaAs.

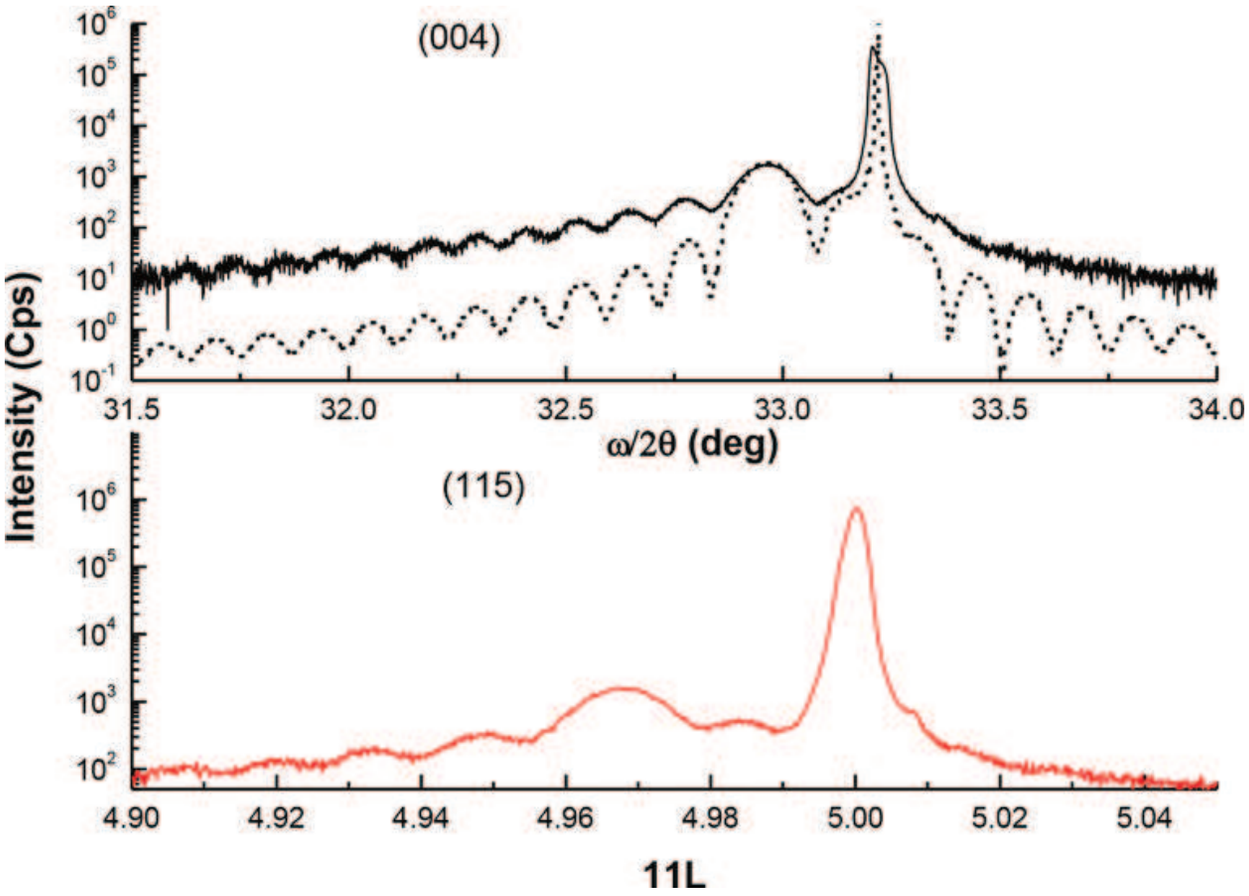

Figure 9. In the top: HRXRD (004) experimental $\omega/2\theta$ curve (solid line) and simulated curve (dotted line) of $GaAs_{0.963}Bi_{0.37}$ layer grown on (100) Zn doped GaAs substrate. In the bottom: optimized scan of HRXRD (11L) reflection plane. L is changed around 5.

The optimization of GaAsBi MOVPE growth conditions was detailed in our previous works [1, 2]. A good crystalline quality was obtained using a V/III ratio of about 9.5, trimethylbismuth (TMBi) flow of 0.2 μmol min^{-1} and a growth temperature of 420°C. The measured Bi content value is around 3.7%. The epitaxial layers show a low Bi island density on the surface [2]. It should be noted that small deviations from optimal growth conditions may give rise to a surface formation of big Bi droplets. The latter appear with a higher density and different shapes for high TMBi flow (~3 μmol min^{-1}).

As a demonstrative example, **Figure 10** illustrates the diffraction patterns of symmetric (004) and asymmetric (115) reflections for the as-grown and annealed GaAsBi layers grown with high TMBi flow. To check thermal stability, GaAsBi layer was annealed at 750°C for 15 min under AsH_3 flow. These curves present more diffraction peaks, other than that of the GaAs substrate, located at 32.8, 32.5 and 32.12° in the left side of the substrate peak, and denoted as GaAsBi(1), GaAsBi(2) and GaAsBi(3), respectively. The same diffraction peaks have been detected in the (115) asymmetric configuration, but more shifted with respect to GaAs

substrate peak. It seems that these three peaks are linked to different Bi contents in GaAsBi layer. Based on the Vegard's law we have found: $x_{GaAsBi(1)}$ = 3.7%, $x_{GaAsBi(2)}$ = 8% and $x_{GaAsBi(3)}$ = 14%. The obtained Bi contents are calculated after the determination of the lattice constants perpendicular and parallel to GaAsBi surface using HRXRD measurements for the (004) and (115) planes, respectively. For hypothetical zinc blend GaBi, the lattice constant is estimated to be 6.324 Å [29]. More calculations details of Bi content are reported in the following Ref. [1]. We have also investigated the structural properties of the annealed layer at 750°C using HRXRD. The measured diffraction curves show a remarkable stability versus thermal annealing. In fact, the same curve shape was obtained for annealed sample (**Figure 10**). Bi droplets are entirely removed from GaAsBi layer after annealing. This behaviour shows that the existence of these droplets is not responsible of diffraction peaks appearance and confirms the structural thermal stability of GaAsBi alloy (**Figure 10**).

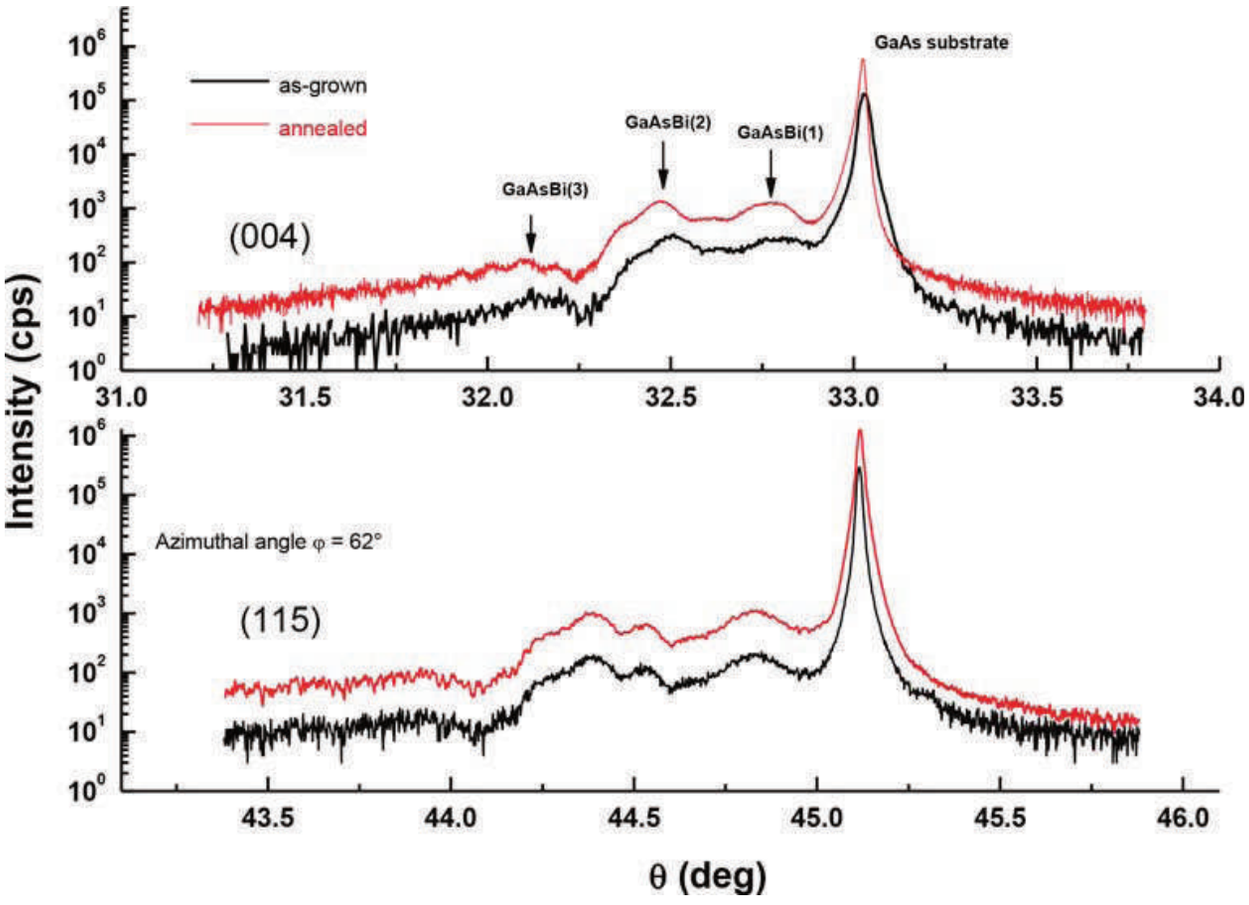

Figure 10. HRXRD (004) and (115) experimental $\omega/2\theta$ patterns of as-grown and annealed GaAsBi layers grown on GaAs substrate at 420°C under 3 μmol min^{-1} of TMBi flow.

To find out an eventual crystallographic tilting of this sample, we have achieved several ω scans for different azimuthal angles φ for each resolved peak indicated by arrows and shown in **Figure 11**. We report in **Figure 11**, for different azimuthal angles, the diffraction angles variation of the substrate $\omega_{Substrate}$ and the layer ω_{GaAsBi} for the three aforementioned peaks (GaAsBi(1), GaAsBi(2) and GaAsBi(3)). All the measured amplitudes of the cosine variation of

http://dx.doi.org/10.5772/65404

$\omega_{Substrate}$ and ω_{GaAsBi} are about 1.18°. Note that the given incertitude on GaAs substrate off cut angle is about 1°, and then the GaAsBi layer is not tilted with respect to the substrate. The splitting between the farthest GaAsBi(004) multiple diffraction peaks is about 0.68°. This value is probably corresponding to a maximum tilt between GaAsBi grains which can be present in the layer.

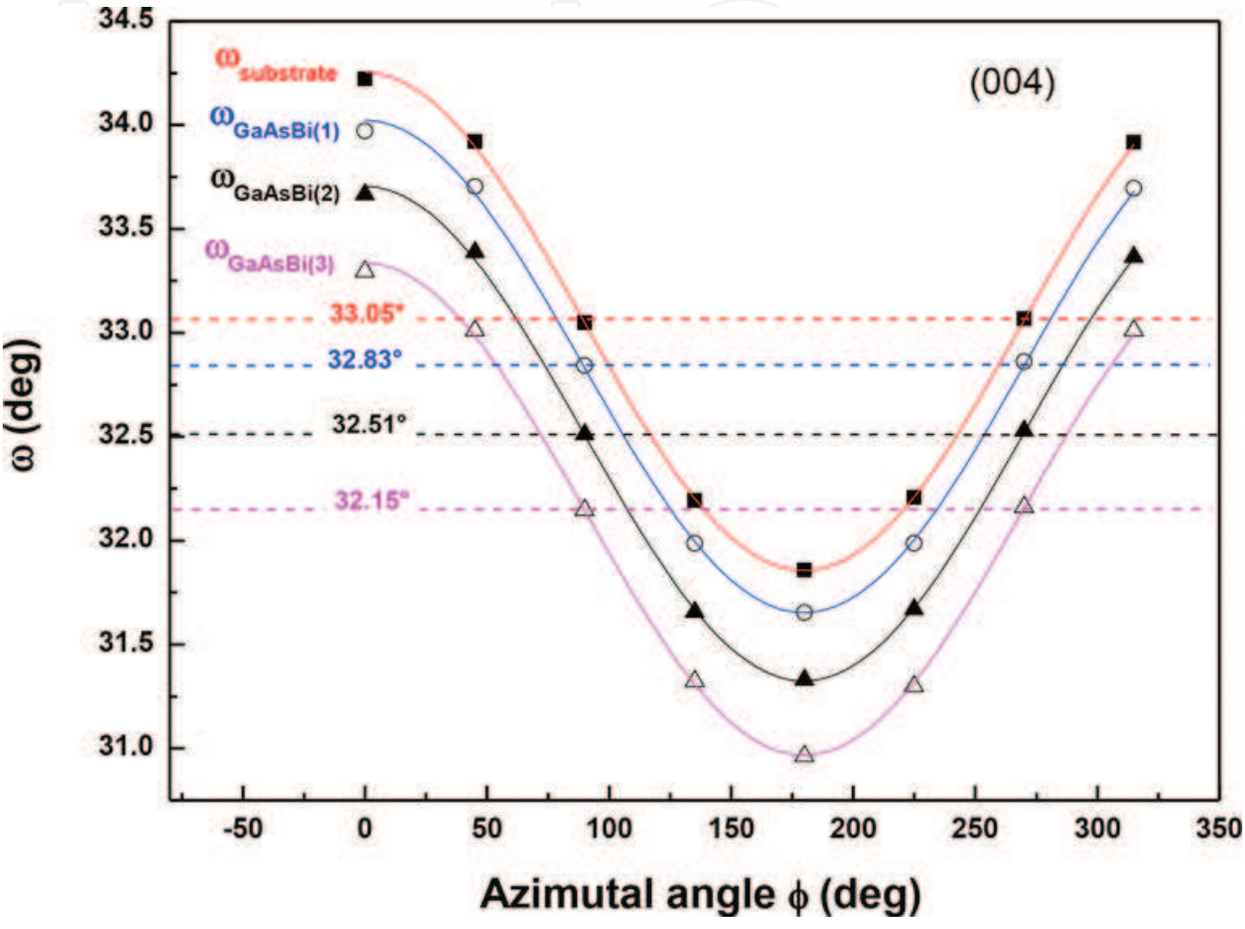

Figure 11. Diffraction angles variation of GaAs substrate (ω_S) and GaAsBi layer (ω_L) for the three aforementioned peaks versus azimuthal angles φ.

Ciatto et al. [30] have investigated the local structure around Bi atoms in GaAsBi layers. Their X-ray absorption spectrometry results show that at 1.2% Bi content, Bi atoms are randomly distributed. At 1.9%, Bi atoms tend to form next-nearest-neighbour pairs, and at 2.4% Bi aggregates appear. In our work, the lowest Bi content in GaAsBi layer is around 3.7%, showing that necessarily Bi aggregates are already formed in the layer.

X-ray diffraction measurements exhibit that growth under high TMBi flow leads to a compositional inhomogeneity, as well as the presence of liquid can affect the Bi incorporation. This fact may be responsible of the XRD pendellösung fringes vanishing, and it was clearly seen when growing GaAsBi under optimized conditions [1, 2]. Some caution is required when interpreting X-ray profile of GaAsBi layers. The confusion can arise from metallic Bi diffraction peak, which can appear in layers having Bi droplet on the surface. Since thermal annealing at

750°C have completely removed Bi islands from the surface, and diffraction curve are exactly the same as before annealing, so this confirms that metallic Bi does not contribute to the diffraction curve.

On interpreting our X-ray profile, the probable assumption is the presence of atomic disorder created by Bi during its incorporation in GaAs matrix. Indeed, the disorder becomes more significant with increasing Bi content. In our case, this content is higher than 3.7% which explains the important disorder and the appearance of several diffraction peaks. There are some assumptions, like support phase separation in GaAsBi alloy [27], the presence of 'micro regions' with different Bi contents [31] or a difference in the strain state at different depths [32].

3.4.2. InGaAs alloys

The lattice mismatch between GaAs and InGaAs alloy layers is relatively small which allows pseudomorphic growth to take place. But uppermost layer can also be partially relaxed or completely relaxed depending on the layer thickness and the indium composition. For a quantitative analysis, the degree of relaxation is given by

$$R = \frac{a_{\text{film}} - a_{\text{substrate}}}{a_{\text{film}}^{\text{relax}} - a_{\text{substrate}}} \tag{14}$$

where a_{film} denotes the measured lattice constant of the film and the totally relaxed lattice constant.R is equal to 1 for fully relaxed films and equal to 0 for pseudomorphic growth.

In this part, we explore a reciprocal space map (RSM) in order to investigate some structural properties of prototype InGaAs alloys in relaxed or strained states.

The Bragg equation relates every X-ray reflex that can be detected with a set of parallel lattice plane (hkl). However, the Laue condition attributes every X-ray reflex to reciprocal lattice point which makes it appropriate to label the reflexes with the indices of their corresponding reciprocal lattice points HKL. The maximum length of the scattering vector in the case of backscattering ($\theta_B = 90°$) is given by $Q_{\max} = 2|k| = \frac{4\pi}{\lambda}$.

Whenever the scattering vector is equal to reciprocal lattice vector, an X-ray reflex is observed. As a result, all reflexes which for a given wavelength λ are accessible for diffraction experiments are situated within the hemisphere with radius equal to $\frac{4\pi}{\lambda}$ (in right of **Figure 12**).

Such a scan can be carried out by combining the $\omega/2\theta$-scan with ω-scan mode in the following way: first for a given length of the scattering angle a ω-scan is accomplished, then the $\omega/2\theta$-scan mode is employed to change the length of the scattering vector by a small amount and then again a ω-scan is performed and shown as reported in left of the **Figure 12**. With RSM measurement, the graph can be presented either in angular coordinates or in reciprocal lattice coordinates. Angular coordinates RSM is the x- and z-axes can be ω, 2θ, $\omega/2\theta$, or $2\theta/\omega$. Reciprocal coordinates RSM shows the graph in reciprocal lattice unit Q_x and Q_z, where can be defined with the following equations [33]:

$$Q_Z = \frac{2}{\lambda}\sin\theta\cos(\omega-\theta)$$
$$Q_X = \frac{2}{\lambda}\sin\theta\sin(\omega-\theta) \quad (15)$$

where λ = 1.5406 Å is the wavelength of $CuK_{\alpha 1}$ radiation, $\theta = 2\theta/2$ the angular position of the detector and ω is the experimental Bragg angle for considered reflection.

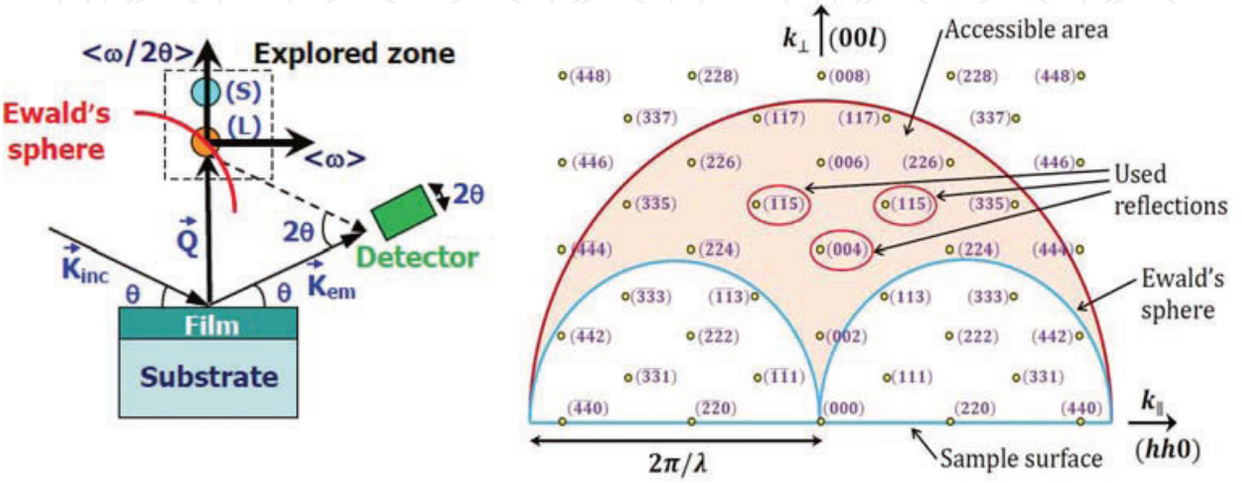

Figure 12. Ewald construction illustrating the scattering geometry in the cases of symmetrical and asymmetrical reflexes. The grey arrows show the scan directions for $\omega/2\theta$-scan and a ω-scan. The accessible reflections in conventional scattering geometry are shown.

ΔQ_Z and ΔQ_X are determined from the difference between measured angles for the substrate and the layer. For (115) reflection on (001) substrate, the perpendicular lattice parameter of the layer is obtained from $\Delta Q_Z = \frac{5}{a_\perp} - \frac{5}{a_s}$
where a_{GaAs}=5.6325 Å is the lattice parameter of the GaAs substrate.

Other possible equivalent representations of reciprocal map are accessible, such as by that representing the Bragg angle change by changing (*hkl*) indices.

Generally, the reciprocal maps show two intense peaks localized in $\Delta Q_X = \Delta Q_Z = 0$ relative to the GaAs substrate and the in $\Delta Q_X \neq \Delta Q_Z \neq 0$ relative to the layer.

3.4.2.1. InGaAs/GaAs relaxed layer

Figure 13 illustrates an example of 2D and 3D map representations for a sample InGaAs/GaAs. In order to analyse maps topography with more facility, pedagogic representation as contour curves of iso-intensity is reported in the same figure.

Using RSM, the analysis of material properties can be completed both qualitatively and quantitatively. The last figure shows the illustration of a qualitative description of the change of the layer peak position with respect to the substrate peak. Qualitatively, a symmetric RSM scan can confirm that our sample is tilted or not. However, to determine whether our sample is strained or relaxed, an asymmetric scan is needed.

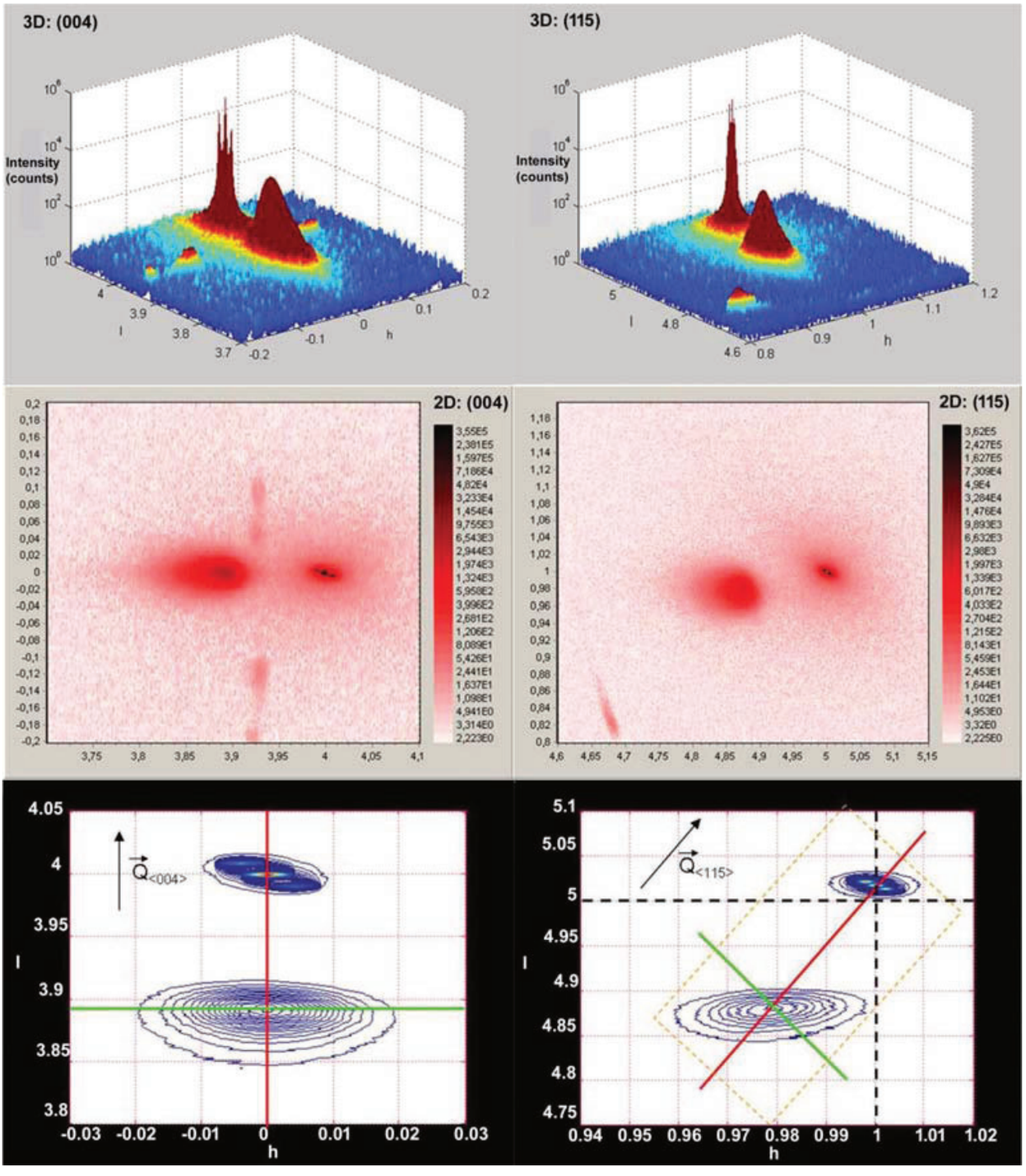

Figure 13. 3D and 2D reciprocal space maps of $In_{.08}Ga_{.92}As/GaAs$ structure, recorded around (004) and (115) nodes. In the bottom, contour curves of iso-intensity are drawn. Diffusion vectors $\vec{Q}_{(004)}$ and $\vec{Q}_{(115)}$ were added to corresponding RSM.

3.4.2.2. InGaAs/GaAs strained layer

InGaAs epitaxial layer on GaAs(100) substrate was investigated by HRXRD in order to determine the structural properties of this strained structure. **Figure 14** shows reciprocal space

http://dx.doi.org/10.5772/65404

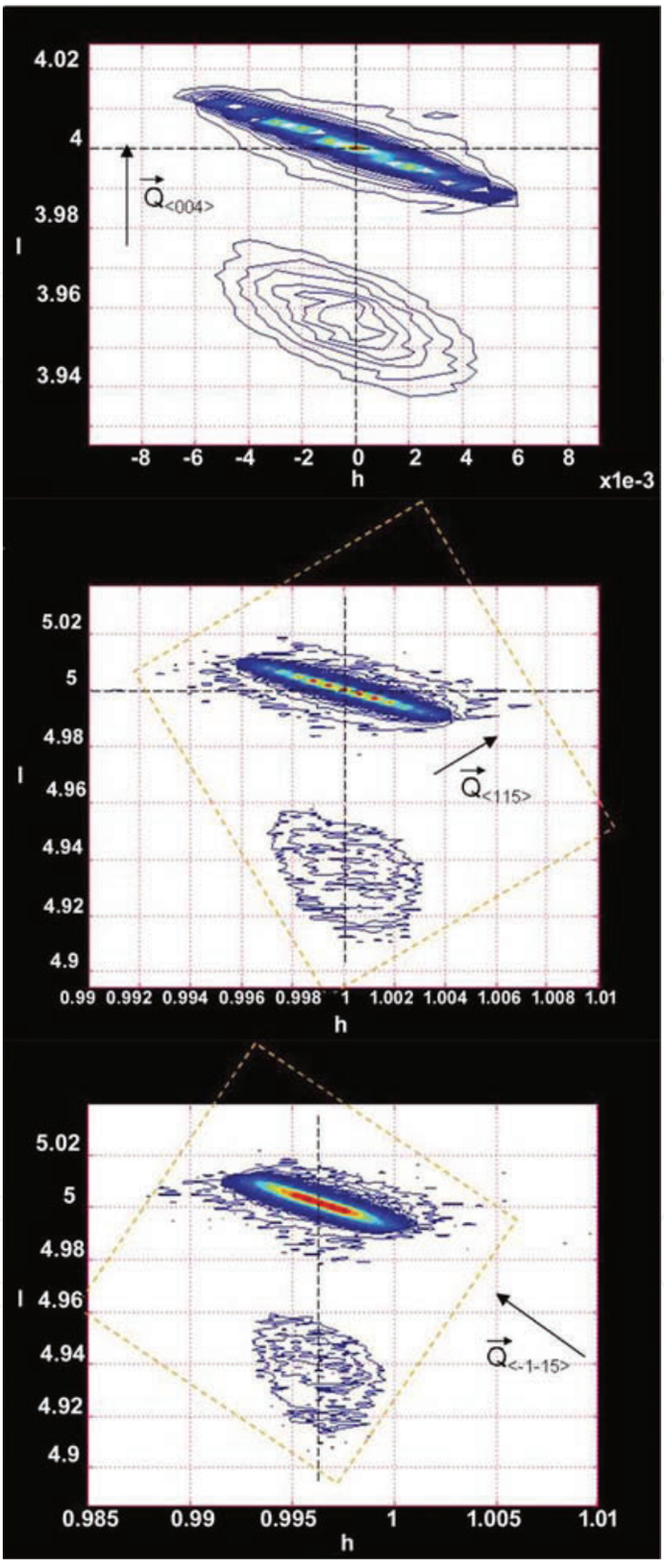

Figure 14. Reciprocal space mapping of $In_{.08}Ga_{.92}As/GaAs$ structure, recorded around (004), (115) and $(\overline{1\bar{1}5})$ nodes. Diffusion vector $\vec{Q}_{(hhl)}$ was added to the corresponding RSM.

maps (RSM) of an InGaAs/GaAs sample in two-dimensional representation of iso-intensity curves around (004), (115) and $(\overline{1\overline{1}5})$ nodes. Note that both spots of InGaAs active layer and GaAs substrate, relative to (004) symmetric reflection, were aligned along <001> direction. The obtained result confirms the absence of tilt between the active layer and the substrate. In addition, diffraction spots from (115) and $(\overline{1\overline{1}5})$ asymmetric reflections were also aligned along the growth direction, which was different from that of scattering vector $\vec{Q}$. Sample was then strained and pseudomorphed. A fully strained epilayer adapts its planar lattice fully with the planar lattice of the substrate (**Figure 14**).

4. Conclusions

This chapter has covered a range of applications of HRXRD technique from simple rocking curve scans (ω and $\omega/2\theta$) to space mapping cartography. Routine measurements applied to particular heterostructures such as GaAs/GaAs(001), GaN/Si(111), GaAsBi/GaAs(001) and InGaAs/GaAs(001) are reported in order to bring the capability of analysis of this technique. The former is a powerful tool that can provide accurate information on the structural properties of the analysed material. Indeed, the method is sensitive enough to determine the composition, thickness and perfection of the epitaxial layers of compound semiconductors.

The application of high-resolution diffraction space mapping is more prevalent since it is now possible to obtain a whole wealth of structural parameters other than just the thickness or composition. This is a developing field and this technique can be considered to determine the deviation from perfection.

Acknowledgements

The authors would like to acknowledge all URHEA members, particularly, Mrs B. El Jani, N. Chaaben, A. Bchetnia and C. Bilel for their help in HRXRD measurements.

Author details

Hédi Fitouri, Mohamed Mourad Habchi and Ahmed Rebey*

*Address all correspondence to: ahmed.rebey@fsm.rnu.tn

Faculty of Sciences, Research Unit on Hetero-Epitaxy and Applications, University of Monastir, Monastir, Tunisia

http://dx.doi.org/10.5772/65404

References

[1] H. Fitouri, I. Moussa, A. Rebey, A. Fouzri, B. El Jani, J. Cryst. Growth 295 (2006), 114–118.

[2] I. Moussa, H. Fitouri, A. Rebey, B. El Jani, Thin Solid Films 516 (2008), 8372–8376.

[3] M. M. Habchi, A. Rebey, B. El Jani, J. Cryst. Growth 310 (2008), 5259–5265.

[4] M. M. Habchi, A. Rebey, B. El Jani, Microelect. J. 39 (2008), 1587–1593.

[5] A. Rebey, L. Béji, B. El Jani, P. Gibart, J. Cryst. Growth 191 (1998), 734–739.

[6] A. Rebey, B. El Jani, A. Leycuras, S. Laugt, P. Gibart, Appl. Phys. 68 (1999), 349–352.

[7] A. Bchetnia, A. Touré, T.A. Lafford, Z. Benzarti, I. Halidou, M.M. Habchi, B. El Jani, J. Cryst. Growth 310 (2008), 5259–5265.

[8] N. Chaaben, T. Boufaden, A. Fouzri, M.S. Bergaoui, B. El Jani, Appl. Surf. Sci. 253 (2006), 241–245.

[9] X. R. Wang, X. Y. Chi, H. Zheng, Z. L. Miao, J. Wang, Z. S. Zhang, Y. S. Jin. J, Vac. Sci. Technol. B 6(1) (1988), 34.

[10] N. Chen, Y. Wang, H. He, L. Lin, Phys. Rev. B. 54(12) (1996), 8516.

[11] W. Lei, M. Pessa, Phys. Rev. B 57(23) (1997), 14627.

[12] A. Rebey, W. Fathallah, B. El Jani, Microelect. J. 37 (2006), 158–166.

[13] A. Rebey, Z. Chine, W. Fathallah, B. El Jani, E. Goovaerts, S. Laugt, Microelect. J. 35 (2004), 875–880.

[14] A. Cremades, L. Görgens, O. Ambacher, M. Stutzmann F. Scholz, Phys. Rev. B 61 (2000), 2812.

[15] V. S. Harutyunyan, A. P. Aivazyan, E. R. Weber, Y. Kim, Y. Park S. G. Subramanya, J. Phys. D: Appl. Phys. 34 (2001), A35–A39.

[16] A. Polian, M. Grimsditcv, I. G. Grzegory, J. Appl. Phys. 79 (1996), 3343.

[17] Z. Chine, A. Rebey, H. Touati, E. Goovaerts, M. Oueslati, B. El Jani, S. Laugt, Phys. Stat. Sol. (A) 203(8) (2006), 1954–1961.

[18] I. H. Lee, I. H. Choi, C. R. Lee, S. K. Noh, Appl. Phys. Lett. 71 (1997), 1359.

[19] P. Gay, P. B. Hirsch, A. Kelly, Acta Met. 1 (1953), 315.

[20] M. J. Hordon, B. L. Averbach, Acta Met. 9 (1961), 237.

[21] J. E. Ayers, J, Cryst. Growth, 135 (1994), 71.

[22] B. Heying, E. J. Tarsa, C. R. Elsass, P. Fini, S. P. DenBaars, J. S. Speck, J. Appl. Phys. 85 (1999), 6470.

[23] Y. Takehara, M. Yoshimoto, W. Huang, J. Saraie, K. Oe, A. Chayahara, Y. Horino, Jpn. J. Appl. Phys. 45 (2006), 67.

[24] S. Tixier, M. Adamcyk, T. Tiedje, S. Francoeur, A. Mascarenhas, P. Wei, F. Schiettekatte, Appl. Phys. Lett. 82 (2003), 2245.

[25] M. Yoshimoto, S. Murata, A. Chayahara, Y. Horino, J. Saraie, K. Oe, Jpn. J. Appl. Phys. 42 (2003), L1235.

[26] K. Oe, J. Cryst. Growth 237–239 (2002), 1481.

[27] K. Oe, Jpn. J. Appl. Phys. 41 (2002), 2801.

[28] K. Oe, H. Okamoto, Jpn. J. Appl. Phys. 37 (1998), L1283.

[29] A. Janotti, S. -H. Wei, S. B. Zhang, Phys. Rev. B 65 (2002), 115203.

[30] G. Ciatto, E. C. Young, F. Glas, J. Chen, R. A. Mori, T. Tiedje, Phy. Rev. B, 78 (2008), 35325.

[31] N. A. El-Masry, E. L. Piner, S. X. Liu, S. M. Bedair, Appl. Phys. Lett. 72 (1998), 40.

[32] S. Pereira, M. R. Correia, E. Pereira, P. O'Donnell, E. Aves, A. D. Sequeira, N. Franco, Appl. Phys. Lett. 79 (2001), 1432.

[33] P. Van der Sluis, J. Phys. D: Appl. Phys. 26 (1993), A188–A191.

Chapter 8

X-Ray Spectroscopy on Biological Systems

Joanna Czapla-Masztafiak, Wojciech M. Kwiatek,
Jacinto Sá and Jakub Szlachetko

Additional information is available at the end of the chapter

http://dx.doi.org/10.5772/64953

Abstract

In the field of biological studies, next to the standard methods, new tools are offered by contemporary physics. X-ray spectroscopic techniques enable probing electronic structure of occupied and unoccupied states of studied atom and distinguish the oxidation state, local geometry, and ligand type of elements that occur in biological material. Direct analysis using X-ray spectroscopy avoids many chemical preparation steps that might modify biological samples. The information obtained gives us insight into important biochemical processes all under physiological conditions. In this chapter we focus our attention to the application of X-ray spectroscopy to the study of biological samples, with special emphasis on mechanisms revealing interaction between DNA and different cytotoxic agents and in the determination of changes in oxidation state of different elements in pathologically altered human cells and tissue.

Keywords: X-ray spectroscopy, XAS, XES, DNA, chemical speciation

1. Introduction

X-ray spectroscopy is a powerful method giving the insight into the chemical and electronic structure of studied samples. Since twentieth century, it has been extensively used in a plethora or research fields starting from solid-state physics [1, 2] and followed by chemical [3] and environmental sciences [4], archeological and art research [5], as well as biological and health studies [6]. The advantages of this technique is its elemental specificity and high penetration depth of probe X-rays resulting in the possibility to undertake *in situ* experiments that provide information about the sample under ambient/operational conditions, that is, direct observation of species at the molecular level in low (biological) concentrations without the need for

preconcentration, extraction, or crystallization [7, 8]. For these reasons, X-ray spectroscopy has been recognized as the valuable addition to classical methods used in biological sciences and many improvements have been made in the experimental techniques as well as data analysis and interpretation. Research includes the simplest systems, such as single compounds, as well as more complex and heterogeneous structures such as cells and tissues. The examples of applications are, among others, the structural characterization of chloroperoxidase compound I [9], the determination of ligand environment of zinc in different tissues of Zn-hyperaccumulating plants [10] and chemical structure of metalloproteins [11]. A lot of researches concern changes in oxidation states of trace elements in case of different pathologically altered cells and tissues, for example the studies of differences in iron and zinc oxidation state contained in healthy and neoplastic tissues of the human brain [12], iron in normal and stenotic human aortic valves [13] or copper inside single neurons from Parkinson's disease and control substantia nigra [14]. Another group of application is identification of elements' chemical species in biological systems, like sulfur in erythrocytes and blood plasma [15], selenium in human cancer cells [16], as well as arsenic in various cell structures [17]. X-ray spectroscopy gives also the opportunity to follow biologically relevant processes in time-resolved experiments including the ultrafast time domain. The processes studied are for example excitation of Mn cluster in photosystem II [18] and recombination of myoglobin following the photolysis of NO [19]. The development of new X-ray sources and X-ray free electron lasers (XFELs) will make possible to study the dynamics of biological systems with femtosecond time resolution, which will elucidate the mechanisms of many important bioprocesses.

The need for more sensitive research methods in medical sciences is forced mostly by the increasing incidence rate of the diseases of affluence, primarily cancer and cardiovascular diseases [20]. These types of studies are focused on two main goals—effective diagnosis on the early stage of the disease and design of efficient therapy. This can be reached, for example, by the discovery and validation of new biomarkers to understand the etiopathology of diseases and by studying new, alternative treatment methods like, for example, novel potential drugs and their interaction with the components of living cells. This review summarizes our latest efforts in applying X-ray spectroscopy to study different biological systems starting from the impact of different damaging agents on the model of DNA molecule and followed by the chemical speciation in the studies of cancerous cell lines and human tissues. Chosen topics show the variety of medically important subjects that can be studied with X-ray spectroscopy and its undeniable role as a technique complementary to classical methods.

2. Principals of X-ray spectroscopy techniques

X-ray spectroscopic methods are atom-specific techniques, using X-ray excitation to gather information about the electronic and geometric structure of the studied system. X-rays in the range from several to few tens of keVs are absorbed by matter mainly through the photoelectric effect. In this process, an X-ray photon with sufficient energy is absorbed by an electron in a tightly bound quantum core level (such as the 1s, 2s or 2p) of an atom. A core electron is promoted to higher, unoccupied state or to the continuum. Following an absorption event, the

atom is in an excited state, with one of the core electron levels left empty (a core hole). During the decay of this intermediate excited state, the core hole is filled by another inner- or valence-shell electron. The decay from the excited to the final state is accompanied by the emission of an X-ray photon, which energy depends on electronic levels involved in the process or by the emission of an Auger electron or Coster-Kroning electron. But the latter phenomenon will not be discussed in this chapter. X-ray absorption and X-ray emission spectroscopy (XAS and XES, respectively) are devoted to the study aforementioned processes. XAS provides information about the unoccupied electronic density of states of an atom whereas XES reflects occupied density of states, and when applied together, providing the detailed picture of the molecular orbitals [21].

The absorption process is described by the absorption coefficient μ in the function of incidence energy, where we can distinguish two regions—a sharp rise in absorption (an absorption edge corresponding to the promotion of the core level electron to the higher state) and the region above absorption edge, characterized by the rich structure. Therefore, XAS spectrum is divided into two parts: the X-ray absorption near-edge structure (XANES)—typically within 30 eV of the main absorption edge, and the extended X-ray absorption fine-structure (EXAFS). XAS spectra are sensitive to the formal oxidation state, coordination chemistry, and the distances, coordination number, and species of the atoms surrounding the selected element. K- and L-level X-ray emission spectra, reflecting the energy distribution of photons emitted by the atoms, can be divided into α and β regions. α lines are characterized by high transition yields but provide little direct chemical information. On the other hand, β lines associated with satellites are being sensitive to chemical environment of the atom, but are much weaker in intensity. For example, two ranges may be recognized around X-ray emission spectrum of Kβ line: Kβ mainline consisting of metal 3p to metal 1s transitions and the valence-to-core (V2C K$\beta_{2,5}$) region comprised of transitions from valence, ligand-localized orbitals to the metal 1s. Both have been shown to contain valuable chemical information—the Kβ mainline is sensitive to the metal spin state as well as the metal-ligand covalence [22] while the V2C region contains information about ligand identity, electronic structure, and metal-ligand bond length [23].

The more detailed information about the electronic structure of studied systems can be obtained by the use of resonant X-ray emission spectroscopy (RXES, also called resonant inelastic X-ray scattering (RIXS)) that is characterized by high sensitivity. RXES, which is photon-in photon-out spectroscopy, combines X-ray absorption and X-ray emission information. RXES experiments can be performed with the use of high-energy resolution X-ray spectrometers, the powerful instruments used to determine the electronic structure of matter that have found many applications in a variety of scientific areas [24–28]. In general, X-ray spectrometers rely on the X-ray dispersion by a crystal providing high-energy resolution for X-ray detection. In order to access detailed information about the electronic structure of matter, the energy resolution has to be around 0.1–5 eV in order to be comparable with the natural lifetimes of studied electronic states of an atom [29, 30]. There are three relevant X-ray emission spectrometer geometries: von Hamos [31, 32], Johannson [33], and Johann [34]. In the RXES studies presented in this review, the von Hamos-type spectrometer has been used with segmented analyzer crystal which disperses the photon energy along one axis and focuses the

X-ray photons along the other axis [35]. Setup scheme for typical RXES experiment under physiological conditions is presented in **Figure 1**.

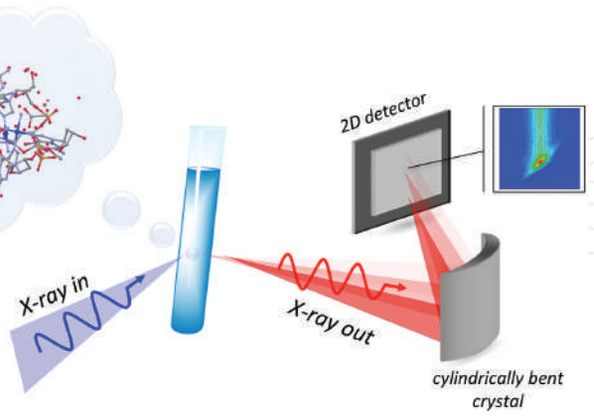

Figure 1. Schematic representation of the experimental setup used in *in situ* RXES experiment [7]. Reproduced by permission of The Royal Society of Chemistry.

The sample is placed at the center of the crystal curvature, and the X-rays are imaged on either a 1D strip detector or a 2D detector. This generates an emission spectrum in a single measurement without any detector or crystal motion. By scanning the incidence energy, one can obtain full RXES plane. A cut in the plane performed at maximum emission energy results in high-resolution X-ray absorption spectrum (HR-XAS) that, due to reduced lifetime broadening, provides detailed information about very small variations in the unoccupied electronic states. The example of RXES plane measured for cisplatin compound is presented in **Figure 2**. It shows the states generated by the resonant excitation of a $2p_{3/2}$ electron into the Pt 5d orbitals (L_3-edge transition). Schematically shown horizontal and vertical cuts along the RXES plane correspond to the $L\alpha_1$ lines of the X-ray emission spectrum (XES) and high-resolution X-ray absorption spectrum (HR-XAS) profiles, which provide information on occupied and unoccupied electronic states of the metal, respectively.

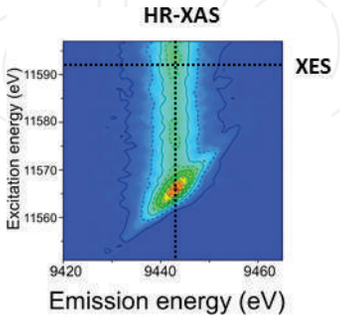

Figure 2. Pt L_3-edge RXES map of cisplatin compound [7]. Reproduced by permission of The Royal Society of Chemistry.

In parallel to the development of the experimental aspects of X-ray spectroscopy, the significant progress has been done in the theory and ab initio calculations of XAS and XES spectra that

enables detailed qualitative and quantitative analysis of experiment. Among others, two representatives of ab initio codes are FEFF9.0 [36] and FDMNES [37]. FEFF9.0, based on Green's Function, is automated software for ab initio multiple scattering calculations of X-ray absorption and X-ray emission signals and various other signals for solids, clusters, or molecules. The code provides yields for X-ray scattering amplitudes that may be directly compared to measured RXES signals. Recently, code was upgraded with several new features for more precise and more realistic calculations, which include ab initio Debye-Waller factors, improved treatment of inelastic loses and core-hole interaction as well as more accurate treatment of crystalline systems with k-space calculations of the Green's function. Similarly, to FEFF software, FDMNES provides yields for X-ray scattering amplitudes that may be directly compared to measured experimental spectra. Nevertheless, unlike FEFF, which is based on self-consistent spherical muffin-tin scattering potentials, the FDMNES employs the finite difference method (FDM) based on density functional theory (DFT) with a potential exchange correlation depending on the local electron density. Therefore, FDMNES may provide more accurate density of states calculations, especially for surface states, but at cost of much longer computation times.

3. Chemical analysis of antitumor compounds

It is beyond doubt that, in case of cancerous diseases, the effective therapy is needed. The majority of drugs used in cancer treatments are cytotoxic (cell killing) and interfere with the cells' DNA. Consequently, the DNA-drug interaction mechanism is of the primary interest when new antitumor compounds are studied. The development of new anticancer drugs is forced by the strong side effects and chemoresistance, both being induced when commonly used platinum-based chemotherapeutics are applied. The binding mechanism of newly synthesized complexes to DNA is one of the most important characteristics to be determined for identification of drug–DNA activity. This can be probed with direct techniques, like nuclear magnetic resonance (NMR) or crystallography. However, these approaches very often require harsh sample preparation that may lead to difficulties in the interpretation of the results. Therefore, simultaneously to the development of new routes of drug synthesis and studying drug-DNA interaction, further development of experimental techniques is necessary. Most importantly, detailed structural and electronic information of the samples has to be retrieved under *in situ* conditions with the ability to control the sample environment and mimicking real physiological conditions.

3.1. Chemical speciation

During the phase of designing new potential antitumor compound, it is important to understand how its structure influences its activity. Especially, it is essential to apprehend why different diastereomers of metal compounds are showing differences in reactivity that sometimes cannot be justified by simple steric effects. In order to study the effect of stereochemistry on the electronic structure around the metal center, RXES technique was used [38]. Two chiral platinum (II) compounds [39], namely (1S,2S)- and (1R,2R)-1-(4-fluorophenyl)-3-

isopropyl-1,2-diaminedichloro platinum(II) (*trans* and *cis*, respectively), were studied. *Cis* isomer exhibits 50-times higher anticancer activity than the *trans* one [39]. Pt L_3-edge RXES spectra of the studied samples were collected with the use of wavelength-dispersive X-ray spectrometer in von Hamos geometry. The experimental setup allows the simultaneous detection of $L\alpha_1$ and valence-to-core (V2C) signals and therefore from obtained maps, HR-XAS and V2C spectra were extracted by performing cuts at RXES plane. Experimental data were complemented with theoretical FEFF9.0 calculations of orbital contribution to the measured signals. This approach gave us the information about the density of occupied and unoccupied electronic states. **Figure 3** presents the comparison of experimental results obtained for *trans* and *cis* compounds.

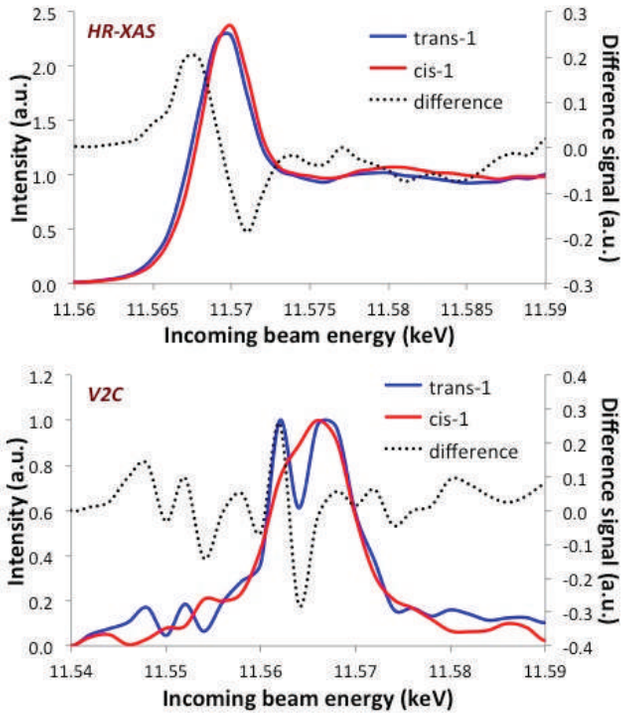

Figure 3. Comparison of the measured HR-XAS (top) and V2C emission (bottom) spectra between *trans* and *cis* Pt-derivatives. Difference profile is the result of subtracting *trans* profile from the *cis* profile [38]. Reproduced by permission of The Royal Society of Chemistry.

Calculated differential signal for both HR-XAS and V2C spectra reveals significant differences that can be associated with the increase of anticancer activity upon configuration inversion from *trans* to *cis*. In case of HR-XAS, the configuration change from *trans* to *cis* shifts the position of the white line to higher energies and increases its intensity, which is caused by increase in empty electronic states. This is related with the increase in the ability to form new bonds and strengthening the formed ones. More pronounced differences can be observed in case of V2C spectra. By analyzing the calculated orbital contributions (**Figure 4**), one can notice that two distinct peaks in V2C *trans* spectrum are resulting from the overlap of filled states of Pt-5d and Cl-2p with F-2p states forming a shoulder. In contrast, in *cis* spectrum, Pt-5d and Cl-2p do not overlap significantly and F-2p orbital is shifted toward higher energy, which results in a loss

of the shoulder and overlap of the two peaks, resolvable in case of *trans* spectrum. The same analysis was performed in order to compare the effect of substitution of various ligands in the studied compounds, and the differences in HR-XAS and V2C spectra were also observed [38] showing that changes in R^1 and R^2 positions influence Pt electronic configuration.

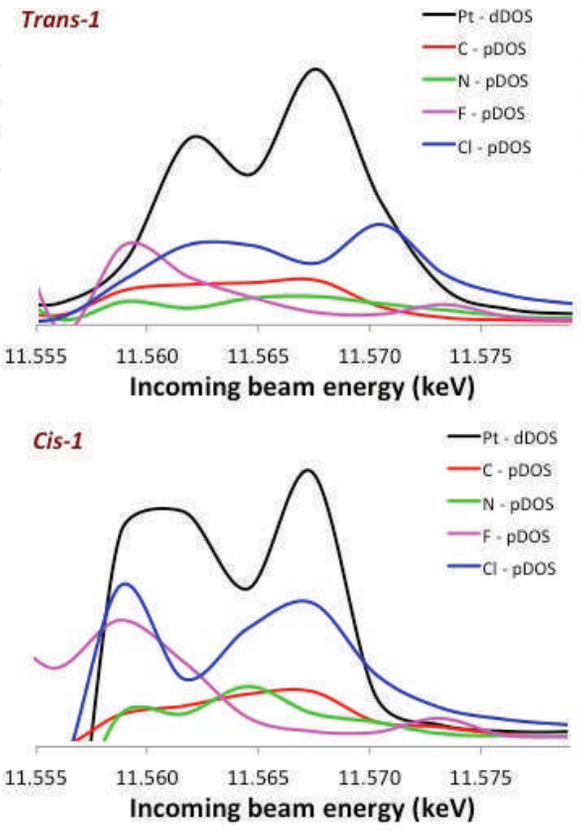

Figure 4. Orbital contribution for V2C emission spectra for *trans* and *cis* Pt-derivatives [38]. Reproduced by permission of The Royal Society of Chemistry.

As it was shown, the RXES technique is sensitive to changes of electronic structure of metallodrugs that arise not only from the changes in the structure of ligands bonded directly to the studied atom but also from the stereochemistry of further neighbors. Therefore, high chemical sensitivity of this method makes it ideal for the studies of anticancer drug mechanism in *in situ/in vivo* conditions.

3.2. The mechanism of action of chemotherapeutic drugs

In further studies, RXES method was also used to disentangle the DNA-drug interaction mechanism [7]. The studies focused on well-known cisplatin (*cis*-diamminedichloroplatinum(II)) compound that is widely used in treating a variety of cancers such as testicular, ovarian, head, and neck tumors [40]. Although very efficient, the use of cisplatin is still dose-limited by side effects and inherited or acquired resistance phenomena, only partially amended by employment of new platinum drugs [41]. Cisplatin action mechanism was only confirmed

via X-ray structural analysis to lead to the formation of intrastrand cross-links (*cis*-[$Pt(NH_3)_2${d(GpG)-N7(1),-N7(2)}]) with DNA 20 years after its implementation [42, 43].

RXES experiment was performed on cisplatin samples incubated for 24 h with calf thymus DNA. In order to follow the full mechanism of cisplatin binding, aqueous and buffer solution (physiological serum) of the drug was also studied. The intensity of the main resonance in the measured RXES Pt L_3-edge map depends directly on the unoccupancy values in the 5d orbitals, which are sensitive to the type of coordinating ligand, bonding strength and angle. Thus, changes in the structure around platinum atom can be easily detected by measuring its density of states in the 5d orbital. *In situ* RXES experiment was combined with theoretical calculations performed with FEFF9.0 code. The differential RXES maps (ΔRXES) resulting from experimental data obtained for cisplatin in aqueous and buffer solution and cisplatin incubated with DNA are presented in **Figure 5(a** and **b**). The results are compared with theoretically calculated spectra for different reaction pathways.

The analysis showed that the hydration of cisplatin in a buffer solution leads to the formation of a mono- and a diaqua complexes (*cis*-$[PtCl(NH_3)_2(H_2O)]^+$ and *cis*-$[Pt(NH_3)_2(H_2O)_2]^{2+}$, respectively). Since both complexes induce similar changes in RXES spectra, it is difficult to judge which of the structures is predominant. Nevertheless, other studies [44, 45] revealed that both structures are likely to play a role in the reaction with DNA. Further, we compare the differential RXES map resulting from the addition of calf thymus DNA to the aquated cisplatin with calculated differences. Calculations were performed for both hydration products and revealed that the final structure of cisplatin–DNA adduct is *cis*-[$Pt(NH_3)_2$-{d(GpG)-N7(1),-N7(2)}], which means that cisplatin bonds to N(7) atoms of adjacent guanines in DNA strand, which is consistent with X-ray crystallography results [42, 43]. Following step in data analysis was the extraction of HR-XAS spectra from RXES maps at constant emission energy of ~9443 eV along with FEFF9.0 calculations of orbital contributions for obtained signals (see **Figure 6**).

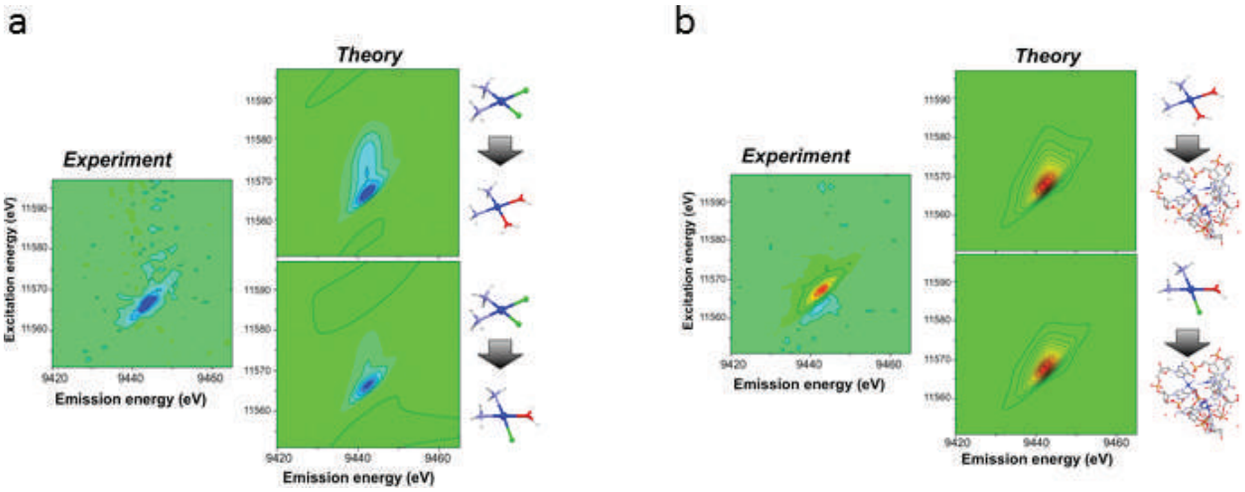

Figure 5. ΔRXES maps resulting from (a) cisplatin hydration in buffer solution. The result is compared with theoretical predictions (top) loss of two chloride ions; and (bottom) loss of a chloride ion, (b) resulting from the bonding of the aquated cisplatin with DNA. The result is compared with theoretical predictions (top) diaqua complex + DNA; and (bottom) monoaqua complex + DNA [7]. Reproduced by permission of The Royal Society of Chemistry.

http://dx.doi.org/10.5772/64953

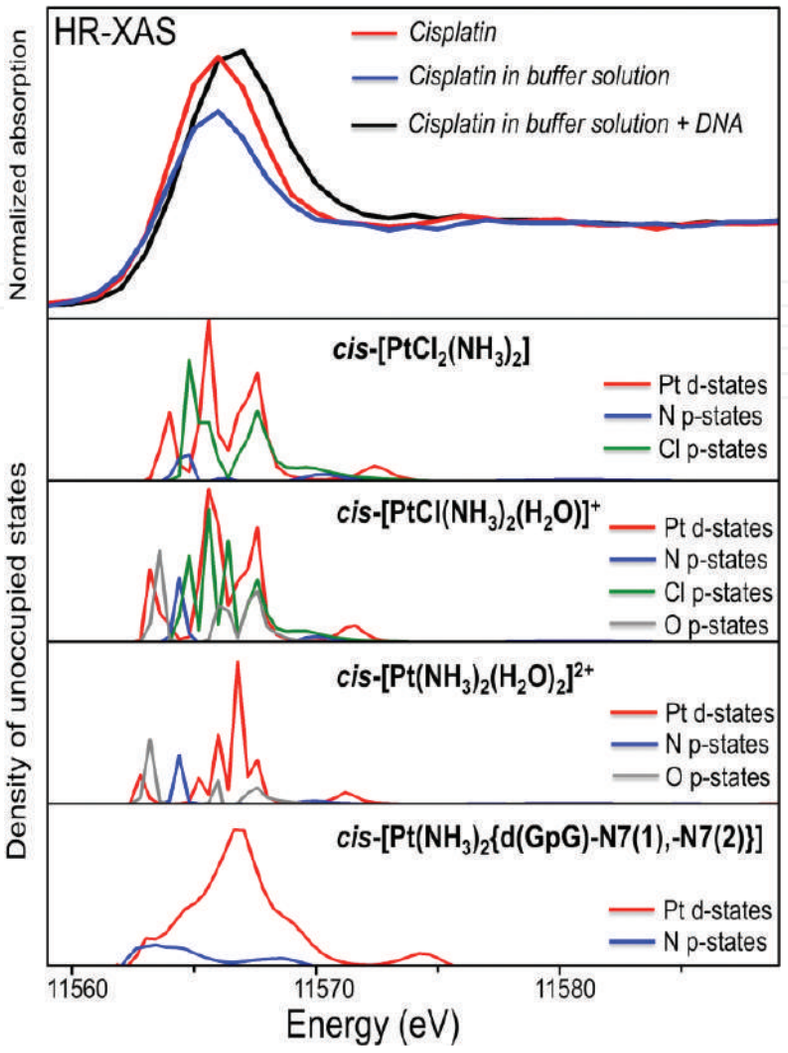

Figure 6. HR-XAS extracted from the RXES maps of (top panel) cisplatin in deionized water (red); cisplatin in buffer solution (blue); and cisplatin in buffer solution + DNA. (black). Pt 5d-density of states orbital contribution computed with FEFF9.0 (subsequent panels) [7]. Reproduced by permission of The Royal Society of Chemistry.

Changes in HR-XAS signal are clearly visible and can be interpreted by the changes in the electronic density of states of platinum and neighboring atoms. In case of hydration products, changes are associated with the substitution of Cl ligands with water molecules that lead to the removal of Cl p-orbital contribution and the appearance of a contribution due to the O p-orbitals from the water molecules that overlap less with Pt d-orbitals indicating weaker bonding. In case of cisplatin-DNA complex, HR-XAS is reflecting strong hybridization of Pt d-orbitals and p-orbitals of N(7) atoms of guanines indicating that the formed bonds are significantly stronger than Pt-Cl (cisplatin) and Pt-O (mono- and diaqua complexes).

The presented methodology has the potential to shorten the time from drug development to drug application by decades because the process is very sensitive and fairly quick, since it does not require extraction and/or preconcentration. The measurements yield direct information of bonding motifs under relevant conditions and in a time-resolved fashion. Furthermore, the

studies can be coupled with the most recent advance in theoretical calculations, which brings an even further dimension when talking about drug action mechanism understanding. RXES provides both basis and confirmation of theoretical study findings, which decreases the computational time tremendously.

We foresee this technique applied to all sorts of systems, and cells as the targets, which is enabled by X-ray probe of high penetration depth and high chemical speciation. The advent of von Hamos dispersive-type spectrometer to follow the system and improved sample delivery systems, such as liquid jet [46], ensures measurements under beam damage-free conditions.

4. Investigating DNA radiation damage

Since many years, more effort is put into the studies of the impact of radiation on human organism. Such research is carried out both in the context of radiation protection and therapy purposes. One of the most important biomolecules being strongly linked to biological radiosensitivity is DNA, which damage may trigger cell death or genomic instability. Common damage types caused by radiation are as follows: single-strand breaks (SSB) and double-strand breaks (DSB), base damage, and DNA-DNA and DNA-protein cross-links. The type and energy of radiation determine the probability of particular kinds of DNA damage production. The interactions of various kinds of radiation with DNA are complex, providing a spectrum of changes that vary in number and distribution. The molecular lesions are caused by either direct ionization/excitation of DNA or indirectly, for example, through the ionization of water and the formation of damaging-reactive hydroxyl radicals. Nevertheless, there are still unanswered questions concerning the detailed mechanism of DNA damage. For instance, the influence of low radiation doses, UV radiation, and the aspect of indirect effects is of particular interest. The biochemical and spectroscopic methods that are commonly used in these kinds of studies can identify the possible damage types and provide information about the timescale for lesion formation, but they are not directly sensitive to the lesion structure. Moreover, these methods typically involve DNA degradation, processing, staining, or labeling procedures, which by themselves may alter the DNA damage [47]. Therefore, a new experimental approach was proposed by us [48] in order to study changes in the molecular structure of the DNA backbone due to the interaction with various radiation types. Using X-ray absorption spectroscopy (XAS) at the phosphorus K-edge, the influence of radiation on both the local geometric and electronic structure around the sugar phosphate backbone was probed. The local structure around the P atoms in DNA is sensitive to the different forms of damage. The DNA strand breaks are linked to bond cleavage in the DNA backbone that can produce 5′-phosphate (5′-PO_4), 3′-phosphate (3′-PO_4), and 3′-phosphoglycolate (3′-PG) termini. Further, the formation of photolesions such as the cyclobutane pyrimidine dimer (CPD) changes the molecular conformation resulting in a distortion around the P atom. In **Figure 7**, the structure of different damage sites is presented.

http://dx.doi.org/10.5772/64953

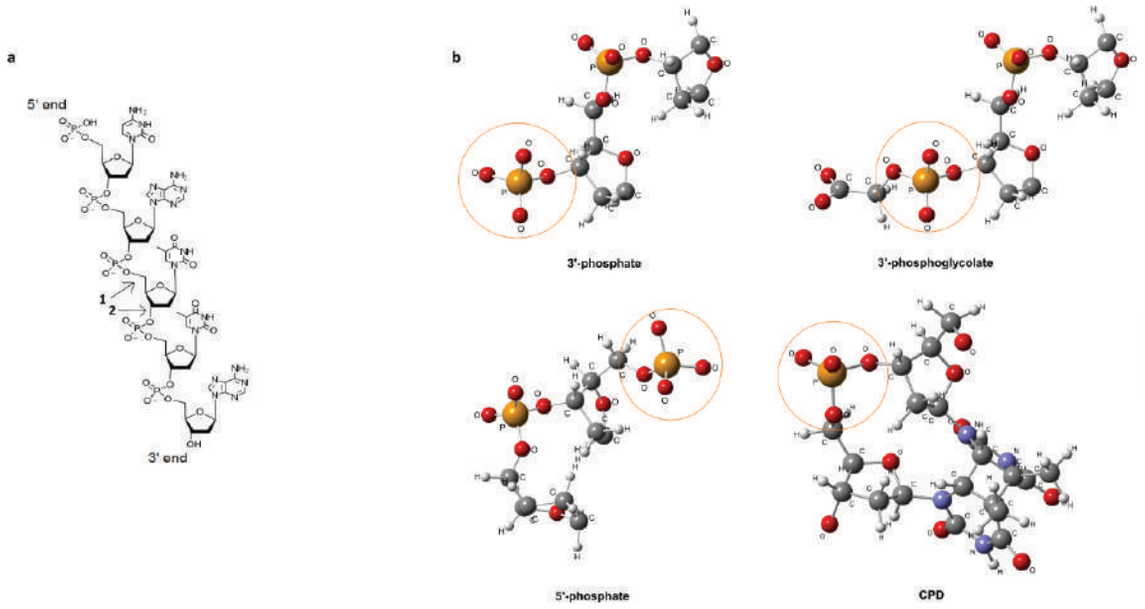

Figure 7. (a) Chemical structure of the fragment of DNA strand. Arrows indicate the bonds that can be broken and lead to 1: 3′-termini; 2: 5′-termini. (b) Structures of the four lesion types: 3′-phosphate, 3′-phosphoglycolate, 5′-phosphate, and CPD. Distorted PO_4 groups are highlighted with orange circles, reproduced from elsewhere with permission [48].

It is expected that various geometries are obtained depending on the form and energy of the radiation used. In our studies, we focused on two different radiation types, namely UV-A and proton radiation. UV-A (315–400 nm) is a main part of UV solar light that is considered as most serious environmental carcinogen. Although its absorption in DNA is rather small, it penetrates our skin very efficiently and can reach its deeper layers [49]. UV-A can cause several damage types and among them the most pronounced are single- and double-strand breaks and CPDs [50], which are produced only by UV radiation. In contrast, proton radiation produces DNA strand breaks but no CPDs. Proton radiation is the most common particle radiation used in cancer therapy of a variety of tumors, including those of the central nervous system, eye, lung, breast, prostate, head, and neck, as well as sarcomas and many pediatric cancers [51]; therefore, its detailed interaction with biomolecules has to be known.

The concept of presented studies [48] was to combine XAS experiment with theoretical calculations in order to identify the damage types and their structure. As a model sample, calf thymus DNA was used because its structure is almost identical with human DNA [52]. X-ray absorption spectra were collected for aqueous solutions of DNA irradiated with UV-A and protons, as well as for non-irradiated DNA that was used as a reference sample. Next, the spectral differences were calculated for P K-edge spectra obtained for irradiated and non-irradiated DNA (**Figure 8(a)**).

Simultaneously, P K-edge XAS spectra were calculated theoretically for each possible damage type (see structures in **Figure 7**), using FDMNES code, and the same procedure, as in case of experimental data, to obtain spectral differences was applied. Among others, the differences showed changes in the intensity of main peak in case of 3′- and 5′-phosphate that can be

associated with the break in one of the C-O bonds around PO_4 group, and a shift toward higher energies in case of CPD structure, associated with decreasing bond angle in O-P-O bond. Next, experimental differences were fitted with theoretical ones. The results of the fit for UV-A irradiated DNA are shown in **Figure 8(b)**. It was shown that the experimental difference can be reconstructed by the combination of theoretical spectra of 3′-phosphate, CPD, and 5′-phosphate with relative ratios 56% (±6.2%), 32% (±12%), and 12% (±6.8%), respectively. It indicates that the major damage types are strand breaks with predominant 3′-phosphate termini structure. Second group of damage is the formation of CPDs, which presence confirms direct absorption of UV-A radiation by DNA molecule. In case of the spectra obtained for proton-irradiated DNA, the same analysis was performed and it revealed that protons produce mainly 3′-phosphate (74% ± 17.6%) and 5′-phosphate (26% ± 19.6%) lesions. No CPDs were detected, supportive with the fact that they are only produced by UV radiation. The results for both irradiation types show that the bond between 5′-carbon atom of deoxyribose and oxygen in the phosphate group is most likely to be broken in the DNA backbone.

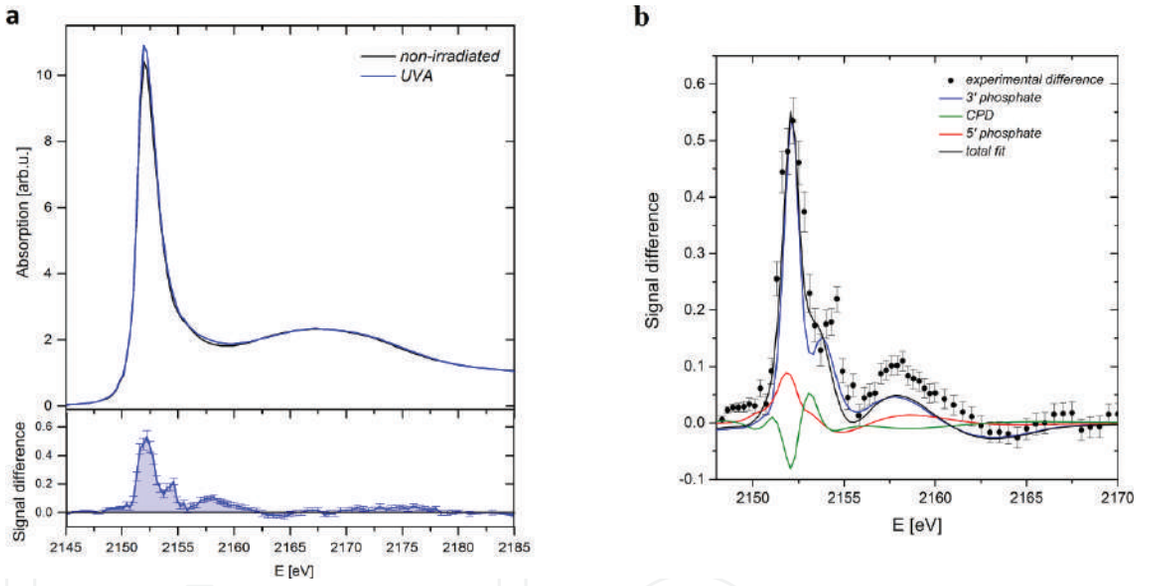

Figure 8. (a) (top) Phosphorus K-edge x-ray absorption spectra of intact and UVA-irradiated aqueous DNA samples; (bottom) P K-edge XAS difference signal between the spectrum of damaged and reference DNA sample. (b) The experimental difference of P K-edge XAS obtained for UVA-irradiated DNA sample fitted with the theoretical spectra. Reproduced from elsewhere with permission [48].

The foregoing approach of determining DNA damage can be easily implemented to study the effect of any damaging agents like various radiation types and chemical compounds. As it was shown, XAS is sensitive to the structure of the produced damage and can provide information about their relative ratios; therefore, it can be used in studies revealing the mechanism of damage development. Especially, it is important to study first stages of damage formation, since, as Boudaïffa et al. [53] suggested, "it is only through a complete understanding of such early events in the generation of genotoxic damage that we may hope to eventually manipulate the effects of ionizing radiation at a molecular level." It is foreseen that the developed methodology can be used in the time-resolved experiments on lesion formation at the X-ray free

electron lasers (XFELs), which give the opportunity to perform X-ray spectroscopy studies with ultrafast timescales.

5. Studies of changes in chemical forms of sulfur in case of prostate cancer

According to the World Health Organization, "cancer is the uncontrolled growth of cells, which can invade and spread to distant sites of the body. Cancer can have severe health consequences and is a leading cause of death" [20]. It comprises 13% of all deaths worldwide and among more than 100 types of cancerous diseases, each requiring unique diagnostic and treatment; prostate cancer is the second most common type in men [20]. As in the case of other cancerous diseases, one of the main issues in prostate cancer research is represented by the discovery and validation of new cancer biomarkers to understand its etiopathology for both diagnosis and new therapies design. A biomarker of cancer can be any structural and/or functional detectable change connected with a cancer disease in human individuals, for example, in genes, proteins, or metabolites [54]. Ideal experimental method to identify such changes should be highly sensitive, specific, and characterized by as minimal as possible sample manipulation. The studies presented in this section take advantage of X-ray spectroscopy to study sulfur species in prostate cancer cell lines and tissue [6, 8, 55, 56]. Sulfur is a key element in human organism. In biological systems, sulfur is present in all of its oxidation state from the reduced one (-2) to the most oxidized one (+6). First of all, it is a part of two amino acids—cysteine and methionine—and their derivatives, which are building blocks of many important proteins. Further, another important compound is the major low-molecular-weight thiol glutathione (GSH), which is involved in the defense against reactive oxygen species that disrupts homeostasis as observed in several pathological conditions [57]. In its oxidized form, sulfur is present for example in sulfates, like chondroitin sulfate, the glucosaminoglycan (GAG) occurring in extracellular matrix that affects proliferation and cell division during growth and differentiation of tissues. Increased expression of chondroitin sulfate is associated with the development of malignant lesions in various tissues, and it was shown that in case of prostate cancer, it indicates high tumor malignancy [58, 59]. Additionally, sulfenic, sulfinic, and sulfonic derivatives may be formed during severe oxidation stress that is strongly associated with cancerogenesis and their presence in prostate cells or their surrounding may indicate dysregulated redox balance [60]. Because of its sensitivity, X-ray absorption spectroscopy accompanied by careful data analysis was applied to such a complex and heterogenic samples.

5.1. Sulfur speciation in prostate cancer cell lines

Commercially available cell lines are often used as a model sample in different cancer research. In the first part of our experiment, three commercial prostate cancer cell lines and one non-cancerous cell lines were used. They were as follows: PC-3 cell line, derived from advanced androgen independent bone metastasized prostate cancer; DU145 cell line, derived from brain metastasis; LNCaP (androgen-sensitive human prostate adenocarcinoma cells), derived from the left supraclavicular lymph node metastasis; and PZ-HPV-7, derived from epithelial cells cultured from normal tissue obtained from the peripheral zone of the prostate. Sulfur K-edge

X-ray absorption spectra were acquired on the paraffin-fixed, dried layer of cells, placed on Mylar foil. Typical spectra obtained for each cell type are presented in **Figure 9(a)**.

All of the spectra are characterized by two strong features at energies 2472.4 and 2480.0 eV that, after the comparison with the spectra of reference compounds [6], were identified as the signature of reduced and oxidized forms of sulfur. Although the positions of the main features are identical in all spectra, they differ by the intensity. Preliminary analysis performed with the use of peak fitting method to determine the area under the peaks showed that the content of reduced sulfur forms does not vary much between cell lines but significant differences are present in the content of oxidized sulfur forms between cancerous and non-cancerous cells [6, 8]. These preliminary results suggested that there might be changes in redox balance, and therefore, the detailed analysis by linear combination fit method was performed with the use of ATHENA software [61]. The method was used before, for example, to establish sulfur forms in erythrocytes and plasma [15]. Experimental S K-edge XAS spectra of prostate cells were fitted with spectra of model sulfur-bearing compounds that are likely to be present in human cells. The chosen groups were as follows: amino acids, thiols, disulfides, sulfonates, and sulfates. In case of sulfonates, two model compounds were used: taurine and cysteic acid. The representative result of fitting procedure is shown in **Figures 9(b)** and **10** presents the results of the fitting for all cell line types in the form of bar graphs together with standard deviation.

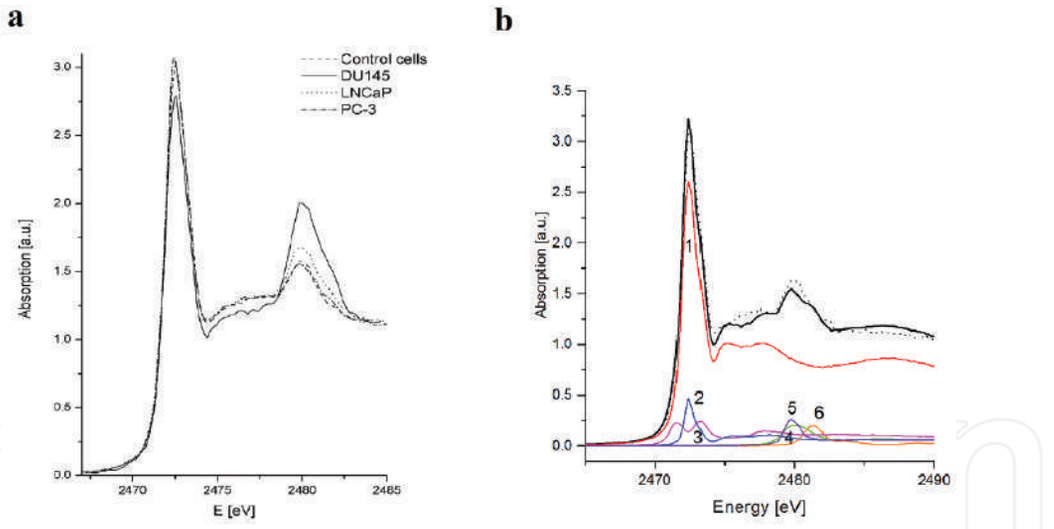

Figure 9. (a) The comparison of experimental S K-edge XANES spectra of four different cell lines. (b) Example of experimental sulfur K-edge XANES spectrum (PC3 cells, dotted line) with a linear combination (solid thick line) of: 1. amino acid, 2. thiol, 3. disulfide, 4. sulfonate (cysteic acid), 5. sulfonate (taurine), and 6. sulfate. Reproduced from elsewhere with permission [8].

In case of disulfide group, no differences were observed. There were very slight changes in amino acids and sulfates content, and the most pronounced differences were shown in case of thiols and sulfonates, especially between DU-145 cells and control cells. Thiols group may be associated mainly with reduced glutathione (GSH) and presented results for this group are consistent with the studies of Canada et al. [62] in which it was shown that DU-145 cells, in

http://dx.doi.org/10.5772/64953

comparison with other prostate cancer cells, are characterized by the highest level of GSH. GSH is known as a neutralizing agent of oxidizing species, produced during severe oxidative stress that is considered as one of the major factors in development and progression of prostate cancer [63]. The higher content might be also the indicator of active cell proliferation as it is observed in cells with aggressive phenotype [64]. The sulfonates group consists mainly of the metabolic products generated during the oxidation of cysteine. The other example is glutathione sulfonate (GSA) that is formed as a result of the interaction between reduced glutathione and free radicals [65].

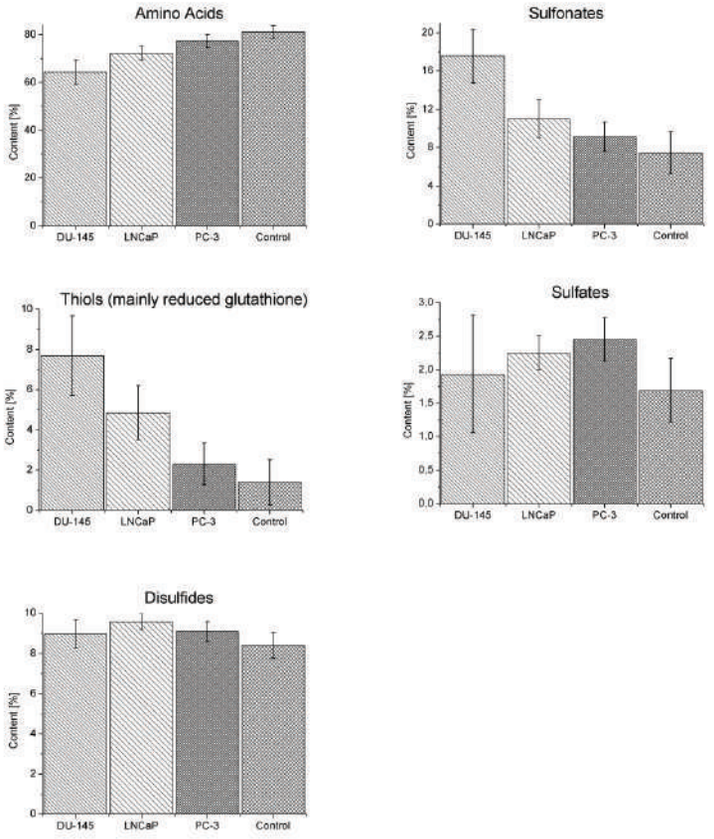

Figure 10. The content of the model groups of compounds in different cell lines obtained from linear combination fit. The sulfonate content represents both cysteic acid and taurine content. The error bars were calculated as the standard deviation of the determined mean values. Reproduced from elsewhere with permission [8].

The results obtained during the analysis of S K-edge XAS spectra of prostate cell lines gave insights into the potential biochemical changes that occur in cancer cells. The differences in the content of thiols between various cancerous cell lines and non-cancerous one may indicate a greater free radical production in cancer cells and their increased proliferative activity. Clearly visible is also the increase in the content of oxidized sulfur forms in case of cancer cells that indicates the unbalanced redox status. Although it is not clear whether these differences are a cause or consequence of malignant transformation, however, the results point out that this process influences strongly the biochemistry of sulfur-bearing compounds inside the cell.

5.2. Distribution of different forms of sulfur in prostate cancer tissue

In prostate tissue, as in other tissues in human organism, we can find different types of cells accompanied by extracellular matrix. Typical prostate is built of two main parts: prostatic glands and stroma composed from smooth muscle cells and connective tissue. Therefore, such a structure is far more complex than cell lines, in which all cells are of the same phenotype. To analyze the distribution of different forms of the element of interest in tissue, XAS imaging can be used and data need to be collected from the tissue area that covers different histological parts. The method is based on the fact that different oxidation states of the same element can be selectively excited by tuning the incidence energy. The generated fluorescence signal is collected in point-by-point mode in the chosen sample area for each of the incidence energy. The fraction of individual forms of the element can be extracted for each pixel by applying the procedure described by Pickering et al. [66, 67]. The calculated relative concentrations can then be used to generate 2D maps of the distribution of each form and compared with microscopic image.

Our experiment [56] was performed on the tissue sections obtained during routine prostatectomies that were in a form of 15-μm-thick air-dried slices placed on Mylar foil. The first step was to measure full XAS spectra in few different points on the tissue in order to establish the value of incidence energies that should be used in XAS imaging. The examples of spectra are presented in **Figure 11**.

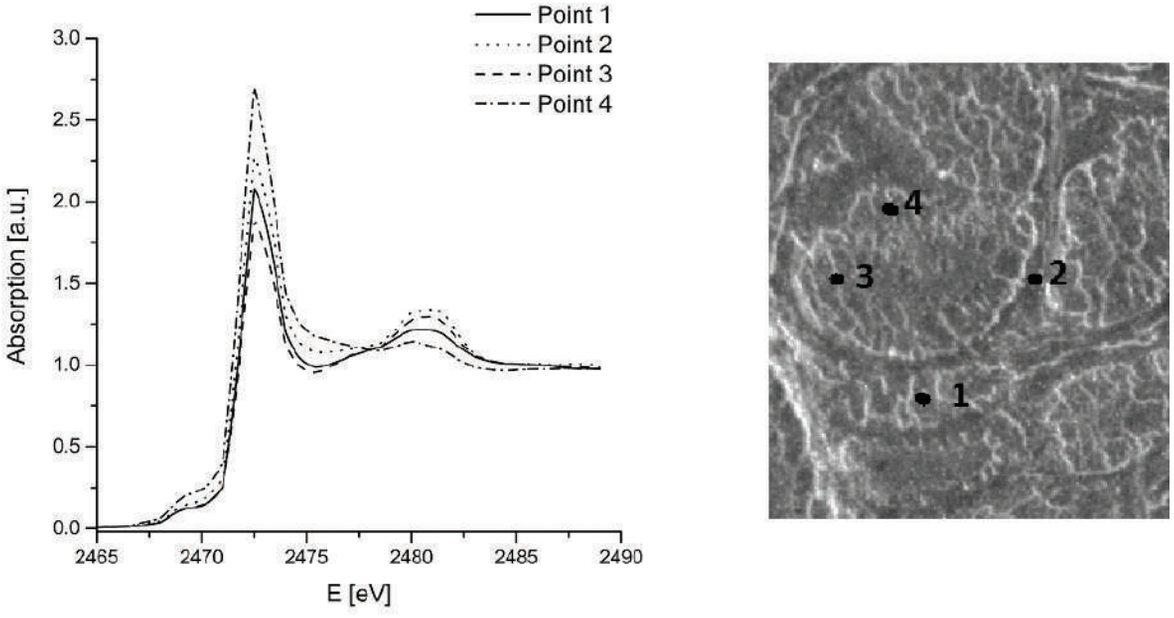

Figure 11. Sulfur K-edge μ-XANES spectra collected at different points in prostate tissue (left) together with the microscopic image of the tissue with marked measurements points (right). Spectra 1, 3, and 4 are measured in nodular part while spectrum 2 in stroma. Reproduced from elsewhere with permission [56].

The two main features have the same energy position as the ones in prostate cancer cells. Therefore, the scanning energies were set above these features (2473 and 2482 eV) to image

http://dx.doi.org/10.5772/64953

reduced and oxidized forms of sulfur in the tissue. Additionally, scans were also performed with energy 2477 eV, which is exciting energy of sulfur with intermediate oxidation state and 2500 eV, which excites total sulfur in the sample. The latter was used to normalize measured fluorescence intensities for different pixels. The data for prostate cancer tissue were collected with 10-μm spatial resolution that was enough to analyze different histological parts. 2D distribution maps of individual chemical forms of sulfur in three prostate cancer tissue samples obtained from three different patients are presented in **Figure 12**. Maps are accompanied by the microscopic image of the studied area.

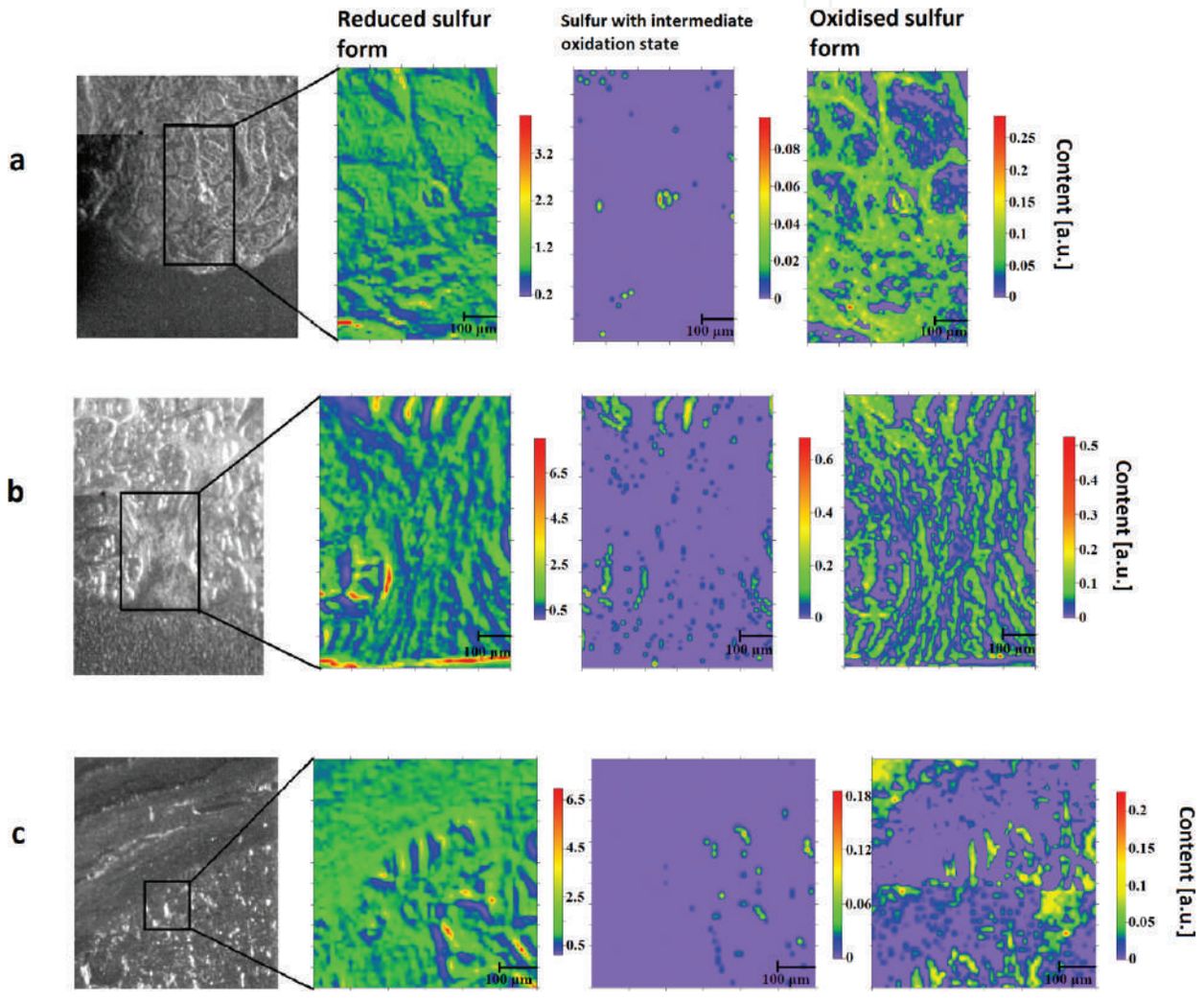

Figure 12. Two-dimensional maps of the distribution of individual chemical forms of sulfur in the selected areas of three different prostate cancer tissue slices together with microscopic image with marked area of scanning. (a–c) Samples derived from three different patients diagnosed with prostate cancer undergoing prostatectomy. Reproduced from elsewhere with permission [56].

Based on the results, we observed that the majority of sulfur located in prostate tissue occurs in reduced form, which is consistent with the results obtained for cell lines. This form is present

in all histological structures but predominantly in glandular part of the tissue. In contrast, the compounds containing sulfur with intermediate oxidation state occur in very small quantities in studied samples and they are not correlated with the specific histological structures. Sulfur with highest oxidation state is distributed unevenly, with higher content present in prostate stroma. As in case of prostate cancer cells, the occurrence of highly oxidized forms of sulfur may be the indicator of the production of oxidative derivatives of sulfur-bearing compounds resulting from the interaction with reactive oxygen species activity due to oxidative stress [60]. But in case of tissue structure, another source of sulfur with high oxidation state may be the elevated concentration of chondroitin sulfate in extracellular matrix, the compound that plays a potential role in aggressiveness of a tumor [58, 59].

Conclusions drawn from this experiment confirmed the results obtained for cell lines and extended them with information about spatial distribution of the various forms of sulfur in different histological parts of tissue. In case of heterogenous samples like human tissue, the methodology applied here allows to study the distribution of various chemical species of the same element without any chemical manipulation. In case of biologically essential elements, the detection of changes in their biochemistry can help to elucidate the possible mechanism of cancer development and progression.

Acknowledgements

Part of this work was supported by the Polish National Science Centre (NCN) under grant No. 2012/05/N/NZ5/00868 and by the European Community's Seventh Framework Program (FP7/2007-2013) under grant agreement No. 290605 (COFUND: PSI-FELLOW).

Author details

Joanna Czapla-Masztafiak[1,2*], Wojciech M. Kwiatek[1], Jacinto Sá[3,4] and Jakub Szlachetko[2,5]

*Address all correspondence to: joanna.czapla@ifj.pan.pl

1 Institute of Nuclear Physics, Polish Academy of Sciences, Krakow, Poland

2 Paul Scherrer Institut, Villigen, Switzerland

3 Department of Chemistry, Ångström Laboratory, Uppsala University, Uppsala, Sweden

4 Institute of Physical Chemistry, Polish Academy of Sciences, Warsaw, Poland

5 Institute of Physics, Jan Kochanowski University in Kielce, Kielce, Poland

References

[1] Szlachetko J, Sá J. Rational design of oxynitride materials: from theory to experiment. CrystEngComm. 2013;15:2583–2587. doi:10.1039/c3ce26909d

[2] Glatzel P, Bergmann U. High resolution 1s core hole X-ray spectroscopy in 3d transition metal complexes—electronic and structural information. Coord. Chem. Rev. 2005;249:65–95. doi:10.1016/j.ccr.2004.04.011

[3] Szlachetko J, Sá J, Nachtegaal M, Hartfelder U, Dousse J-C, Hoszowska J et al. Real time determination of the electronic structure of unstable reaction intermediates during Au_2O_3reduction. J. Phys. Chem. Lett. 2014;5:80–84. doi:10.1021/jz402309s

[4] Schäfer T, Buckau G, Artinger R, Kim JI, Geyer S, Wolf M et al. Origin and mobility of fulvic acids in the Gorleben aquifer system: implications from isotopic data and carbon/sulfur XANES. Org. Geochem. 2005;36:567–582. doi:10.1016/j.orggeochem.2004.10.011

[5] Nakai I, Matsunaga M, Adachi M, Hidaka K-I. Application of XAFS in archaeology. Journal de Physique IV Colloque. 1997;7:pp. C2-1033 – C2-1034. doi:10.1051/jp4:19972131

[6] Czapla J, Kwiatek WM, Lekki J, Steininger R, Göttlicher J. Determination of changes in sulphur oxidation states in prostate cancer cells. Acta Phys. Pol. A. 2012;121:497–501. doi:10.12693/APhysPolA.121.497

[7] Lipiec E, Czapla J, Szlachetko J, Kayser Y, Kwiatek W, Wood B, et al. Novel *in situ* methodology to observe the interactions of chemotherapeutical Pt drugs with DNA under physiological conditions. Dalton Trans. 2014;43:13839–44. doi:10.1039/c4dt00861h

[8] Czapla J, Kwiatek WM, Lekki J, Dulińska-Litewka J, Steininger R, Göttlicher J. Chemical species of sulfur in prostate cancer cells studied by XANES spectroscopy. Rad. Phys. Chem. 2013;93:154–159. doi:10.1016/j.radphyschem.2013.05.021

[9] Stone KL, Behan RK, Green MT. X-ray absorption spectroscopy of chloroperoxidase compound I: insight into the reactive intermediate of P450 chemistry. Proc. Natl. Acad. Sci. U.S.A. 2005;102:16563–16565. doi:10.1073/pnas.0507069102

[10] Salt DE, Prince RC, Baker AJM, Raskin I, Pickering IJ. Zinc ligands in the metal hyperaccumulator Thlaspi caerulescens as determined using X-ray absorption spectroscopy. Environ. Sci. Technol. 1999;33:713–717. doi:10.1021/es980825x

[11] Arcovito A, Benfatto M, Cianci M, Hasnain SS, Nienhaus K, Nienhaus GU, et al. X-ray structure analysis of a metalloprotein with enhanced active-site resolution using *in situ* X-ray absorption near edge structure spectroscopy. Proc. Natl. Acad. Sci. U. S. A. 2007;104:6211–6216. doi:10.1073/pnas.0608411104

[12] Wandzilak A, Czyzycki M, Wrobel P, Szczerbowska-Boruchowska M, Radwanska E, Adamek D, et al. The oxidation states and chemical environments of iron and zinc as

potential indicators of brain tumour malignancy grade—preliminary results. Metallomics. 2013;5:1547–1553. doi:10.1039/c3mt00158j

[13] Czapla-Masztafiak J, Lis GJ, Gajda M, Jasek E, Czubek U, Bolechała F, et al. Determination of oxidation state of iron in normal and pathologically altered human aortic valves. Nucl. Instruments Methods Phys. Res. Sect. B. 2015;364:70–75. doi:10.1016/j.nimb.2015.04.026

[14] Chwiej J, Adamek D, Szczerbowska-Boruchowska M, Krygowska-Wajs A, Bohic S, Lankosz M. Study of Cu chemical state inside single neurons from Parkinson's disease and control substantia nigra using the micro-XANES technique. J. Trace Elem. Med. Biol. 2008;22:183–188. doi:10.1016/j.jtemb.2008.03.006

[15] Pickering IJ, Prince RC, Divers T, George GN. Sulfur K-edge X-ray absorption spectroscopy for determining the chemical speciation of sulfur in biological systems. FEBS Lett. 1998;441:11–14. doi:10.1016/S0014-5793(98)01402-1

[16] Weekley CM, Aitken JB, Vogt S, Finney L a., Paterson DJ, De Jonge MD, et al. Uptake, distribution, and speciation of selenoamino acids by human cancer cells: X-ray absorption and fluorescence methods. Biochemistry. 2011;50:1641–1650. doi:10.1021/bi101678a

[17] Bacquart T, Deves G, Ortega R. Direct speciation analysis of arsenic in sub-cellular compartments using micro-X-ray absorption spectroscopy. Environ. Red. 2010;110:413–416. doi:10.1016/j.envres.2009.09.006

[18] Dau H, Haumann M. Time-resolved X-ray spectroscopy leads to an extension of the classical S-state cycle model of photosynthetic oxygen evolution. Photosynth. Res. 2007;92:327–343. doi:10.1007/s11120-007-9141-9

[19] Lima FA, Milne CJ, Amarasinghe DC V, Rittmann-Frank MH, Veen RM Van Der, Reinhard M, et al. A high-repetition rate scheme for synchrotron-based picosecond laser pump X-ray probe experiments on chemical and biological systems in solution. Rev. Sci. Instrum. 2011;82:063111. doi:10.1063/1.3600616

[20] Available from: http://www.who.int/cancer/en/ [Accessed: 11.07.2016]

[21] Sá J. High-resolution XAS/XES: analyzing electronic strudtures of catalysis. CRC Press: Taylor and Francis Group; 2014.

[22] Lundberg M, Kroll T, DeBeer S, Bergmann U, Wilson S, Glatzel P, et al. Metal-ligand covalency of iron complexes from high-resolution resonant inelastic X-ray scattering. J. Am. Chem. Soc. 2013;135:17121–17134. doi:10.1021/ja408072q

[23] Pollock CJ, DeBeer S. Valence-to-core X-ray emission spectroscopy: a sensitive probe of the nature of a bound ligand. J. Am. Chem. Soc. 2011;133:5594–5601. doi:10.1021/ja200560z

[24] Vankó G, Renz F, Molnár G, Neisius T, Kárpáti S. Hard-X-ray-induced excited-spin-state trapping. Angew. Chemie Int. Ed. 2007;46:5306–5309. doi:10.1002/anie.200604432

[25] Bergmann U, Glatzel P. X-ray emission spectroscopy. Photosynth. Res. 2009;102:255–266. doi:10.1007/s11120-009-9483-6

[26] Sikora M, Juhin A, Weng T-C, Sainctavit P, Detlefs C, de Groot F, et al. Strong K-edge magnetic circular dichroism observed in photon-in-photon-out spectroscopy. Phys. Rev. Lett. 2010;105:037202. doi:10.1103/PhysRevLett.105.037202

[27] Singh J, Lamberti C, van Bokhoven J. Advanced X-ray absorption and emission spectroscopy: *in situ* catalytic studies. Chem. Soc. Rev. 2010;39:4754–4766. doi:10.1039/c0cs00054j

[28] Lancaster KM, Roemelt M, Ettenhuber P, Hu Y, Ribbe MW, Neese F, et al. X-ray emission spectroscopy evidences a central carbon in the nitrogenase iron-molybdenum cofactor. Science. 2011;334:974–977. doi:10.5061/dryad.6m0f6870

[29] Campbell JL, Papp T. Atomic level widths for X-ray spectrometry. X-ray Spetrom. 1995;24:307–319. doi:10.1002/xrs.1300240606

[30] Campbell JL, Papp T. Widths of the atomic K-N7 levels. At. Data Nucl. Data Tables. 2001;77:1–56. doi:10.1006/adnd.2000.0848

[31] von Hámos L. X-ray spectroscopy and imaging by means of a curved crystal reflectors. Naturwissenschaften. 1932;20:705.

[32] Hoszowska J, Dousse JC, Kern J, Rheme C. High-resolution von Hamos crystal X-ray spectrometer. Nucl. Instrum. Methods Phys. Res. Sect. A. 1996;376:129–138. doi:10.1016/0168-9002(96)00262-8

[33] Johannson T. On a novel, exactly focusing X-ray spectrometer. Zeitschrift Für Phys. 1931;82:507.

[34] Johann HH. Obtaining intense X-ray spectra by means of concave crystals. Zeitschrift Für Phys. 1931;69:185.

[35] Szlachetko J, Nachtegaal M, De Boni E, Willimann M, Safonova O, Sà J, et al. A von Hamos X-ray spectrometer based on a segmented-type diffraction crystal for single-shot X-ray emission spectroscopy and time-resolved resonant inelastic X-ray scattering studies. Rev. Sci. Instrum. 2012;83:103105. doi:10.1063/1.4756691

[36] Rehr JJ, Kas JJ, Vila FD, Prange MP, Jorissen K. Parameter-free calculations of X-ray spectra with FEFF9. Phys. Chem. Chem. Phys. 2010;12:5503–5513. doi:10.1039/b926434e

[37] Bunău O, Joly Y. Self-consistent aspects of X-ray absorption calculations. J. Phys. Condens. Matter. 2009;21:345501. doi:10.1088/0953-8984/21/34/345501

[38] Sá J, Czapla-Masztafiak J, Lipiec E, Kayser Y, Fernandes DLA, Szlachetko J, et al. Resonant X-ray emission spectroscopy of platinum(ii) anticancer complexes. Analyst. 2016;141:1226–1232. doi:10.1039/C5AN02490K

[39] Berger G, Leclercqz H, Derenne A, Gelbcke M, Goormaghtigh E, Nève J, et al. Synthesis and in vitro characterization of platinum(II) anticancer coordinates using FTIR spectroscopy and NCI COMPARE: a fast method for new compound discovery. Bioorg. Med. Chem. 2014;22:3527–3536. doi:10.1016/j.bmc.2014.04.017

[40] Tisato F, Marzano C, Porchia M, Pellei M, Santini C. Copper in diseases and treatments, and copper-based anticancer strategies. Med. Res. Rev. 2010;30:708–749. doi:10.1002/med.20174

[41] Santini C, Pellei M, Gandin V, Porchia M, Tisato F, Marzano C. Advances in copper complexes as anticancer agents. Chem. Rev. 2014;114:815–862. doi:10.1021/cr400135x

[42] Sherman SE, Gibson D, Wang AH-J, Lippard SJ. X-ray structure of the major adduct of the anticancer drug cisplatin with DNA: cis-[Pt(NH3)2(d(pGpG))]. Science. 1985;230:412–417. doi:10.1126/science.4048939

[43] Takahara P, Rosenzweig A, Frederick C, Lippard S. Crystal structure of double-stranded DNA containing the major adduct of the anticancer drug cisplatin. Nature. 1995;377:649–652. doi:10.1038/377649a0

[44] Baik MH, Friesner RA, Lippard SJ. Theoretical study of cisplatin binding to purine bases: why does cisplatin prefer guanine over adenine? J. Am. Chem. Soc. 2003;125:14082–14092. doi:10.1021/ja036960d

[45] Cepeda V, Fuertes M, Castilla J, Alonso C, Quevedo C, Pérez JM. Biochemical mechanisms of cisplatin cytotoxicity. Anticancer. Agents Med. Chem. 2007;7:3–18. doi:10.2174/187152007779314044

[46] Fernandes DLA, Pavliuk MV, Sá J. A 3D printed microliquid jet with an adjustable nozzle diameter. Analyst. 2015;140:6234–6238. doi:10.1039/C5AN01329A

[47] Jiang Y, Rabbi M, Kim M, Ke C, Lee W, Clark RL, et al. UVA generates pyrimidine dimers in DNA directly. Biophys J. 2009;96:1151–1158. doi:10.1016/j.bpj.2008.10.030

[48] Czapla-Masztafiak J, Szlachetko J, Milne CJ, Lipiec E, Sá J, Penfold TJ, et al. Investigating DNA radiation damage using X-ray Absorption Spectroscopy (XAS). Biophys. J. 2016;110:1304–1311. doi:10.1016/j.bpj.2016.01.031

[49] Osipov AN, Smetanina NM, Pustovalova MV, Arkhangelskaya E, Klokov D. The formation of DNA single-strand breaks and alkali-labile sites in human blood lymphocytes exposed to 365-nm UVA radiation. Free Radic. Biol. Med. 2014;73:34–40. doi:10.1016/j.freeradbiomed.2014.04.027

[50] Kielbassa C, Roza L, Epe B. Wavelength dependence of oxidative DNA damage induced by UV and visible light. Carcinogenesis. 1997;18:811–816. doi:10.1093/carcin/18.4.811

[51] Foote RL, Stafford SL, Petersen IA, Pulido JS, Clarke MJ, Schild SE, et al. The clinical case for proton beam therapy. Radiat. Oncol. 2012;7:174–183. doi:10.1186/1748-717X-7-174

[52] Mouret S, Philippe C, Gracia-Chantegrel J, Banyasz A, Karpati S, Markovitsi D, et al. UVA-induced cyclobutane pyrimidine dimers in DNA: a direct photochemical mechanism? Org. Biomol. Chem. 2010;8:1706–1711. doi:10.1039/b924712b

[53] Boudaïffa B, Cloutier P, Hunting D, Huels M a, Sanche L. Resonant formation of DNA strand breaks by low-energy (3 to 20 eV) electrons. Science. 2000;287:1658–1660. doi:10.1126/science.287.5458.1658

[54] Bellisola G, Sorio C. Infrared spectroscopy and microscopy in cancer research and diagnosis. Am. J. Cancer Res. 2012;2:1–21.

[55] Kwiatek WM, Czapla J, Podgórczyk M, Kisiel A, Konior J, Balerna A. First approach to studies of sulphur electron DOS in prostate cancer cell lines and tissues studied by XANES. Rad. Phys. Chem. 2011;80:1104–1108. doi:10.1016/j.radphyschem.2011.05.005

[56] Czapla-Masztafiak J, Okoń K, Gałka M, Huthwelker T, Kwiatek WM. Investigating the distribution of chemical forms of sulfur in prostate cancer tissue using X-ray absorption spectroscopy. Appl. Spectrosc. 2016;70:264–271. doi:10.1177/0003702815620128

[57] Matés JM, Segura JA, Alonso FJ, Márquez J. Pathways from glutamine to apoptosis. Front. Biosci. 2006;11:3164–3180.

[58] Ricciardelli C, Mayne K, Sykes PJ, Raymond WA, McCaul K, Marshall VR, et al. Elevated stromal chondroitin sulfate glycosaminoglycan predicts progression in early-stage prostate cancer. Clin. Cancer Res. 1997;3:983–992.

[59] Ricciardelli C, Quinn DI, Raymond WA, McCaul K, Sutherland PD, Stricker PD, et al. Elevated levels of peritumoral chondroitin sulfate are predictive of poor prognosis in patients treated by radical prostatectomy for early-stage prostate cancer. Cancer Res. 1999;59:2324–2328.

[60] Paschos A, Pandya R, Duivenvoorden WCM, Pinthus JH. Oxidative stress in prostate cancer: changing research concepts towards a novel paradigm for prevention and therapeutics. Prostate Cancer Prostatic Dis. 2013;16:217–225. doi:10.1038/pcan.2013.13

[61] Ravel B, Newville M. ATHENA, ARTEMIS, HEPHAESTUS: data analysis for X-ray absorption spectroscopy using IFEFFIT. J. Synchrotron Radiat. 2005;12:537–541. doi:10.1107/S0909049505012719

[62] Canada AT, Roberson KM, Vessella RL, Trump DL, Robertson CN, Fine RL. Glutathione and glutathione S-transferase in benign and malignant prostate cell lines and prostate tissues. Biochem. Pharmacol. 1996;51:87–90. doi:10.1016/0006-2952(95)02157-4

[63] Khandrika L, Kumar B, Koul S, Maroni P, Koul HK. Oxidative stress in prostate cancer. Cancer Lett. 2009;282:125–136. doi:10.1016/j.canlet.2008.12.011

[64] Matés JM, Pérez-Gómez C, De Castro IN, Asenjo M, Márquez J. Glutamine and its relationship with intracellular redox status, oxidative stress and cell proliferation/death. Int. J. Biochem. Cell Biol. 2002;34:439–458. doi:10.1016/S1357-2725(01)00143-1

[65] Wefers H, Sies H. Oxidation of glutathione by the superoxide radical to the disulfide and the sulfonate yielding singlet oxygen. Eur. J. Biochem. 1983;137:29–36.

[66] Pickering IJ, Sneeden EY, Prince RC, Block E, Harris HH, Hirsch G, et al. Localizing the chemical forms of sulfur in vivo using X-ray fluorescence spectroscopic imaging: application to onion (*Allium cepa*) tissues. Biochemistry. 2009;48:6846–6853. doi:10.1021/bi900368x

[67] Pickering IJ, George GN. X-ray absorption spectroscopy imagin of biological tissues. AIP Conf. Proc. 2007;882:311–315. doi:10.1063/1.2644509

Chapter 9

X-Ray Diffraction in Biology: How Can We See DNA and Proteins in Three Dimensions?

Claudine Mayer

Additional information is available at the end of the chapter

http://dx.doi.org/10.5772/64999

Abstract

Knowing the three-dimensional structure of biological macromolecules, such as proteins and DNA, is crucial for understanding the functioning of life. Biological crystallography, the main method of structural biology, which is the branch of biology that studies the structure and spatial organization in biological macromolecules, is based on the study of X-ray diffraction by crystals of macromolecules. This article will present the principle, methodology and limitations of solving biological structures by crystallography.

Keywords: biological macromolecules, X-ray diffraction, monocristal, tridimensional structure

1. Introduction

In 1953, James Watson and Francis Crick revealed the double helical structure of DNA using the results of Rosalyn Franklin obtained by X-ray scattering on natural filaments formed by DNA molecules [1]. Proteins, the nanomachines essential to living organisms, have their "manufacturing plan" encoded in their DNA gene sequence [2]. During their synthesis, proteins adopt a specific three-dimensional structure that allows them to perform their functions within the cell. "Seeing" the structure of biological macromolecules, such as proteins or nucleic acids (RNA or DNA), allows researchers to elucidate the mechanisms of live in all organisms, and among many other applications, allows them to design new drugs [3].

"Seeing" proteins or nucleic acids in three dimensions, a dream or a reality? Could microscopy, a technic known since more than 350 years that allows to visualize biological cells, be the right

approach? Of course, the dimensions of these two objects, macromolecules and cells are very different: The cell size ranges generally from 10 to 100 microns (10^{-6} m), the dimensions of biological macromolecules, proteins or nucleic acids, are of the order of tens of angstroms (10^{-10} m) (**Figure 1**). To reach atomic details, the method of choice is crystallography, whose principle is based on the bombardment by X-ray of crystals composed of biological macromolecules [4].

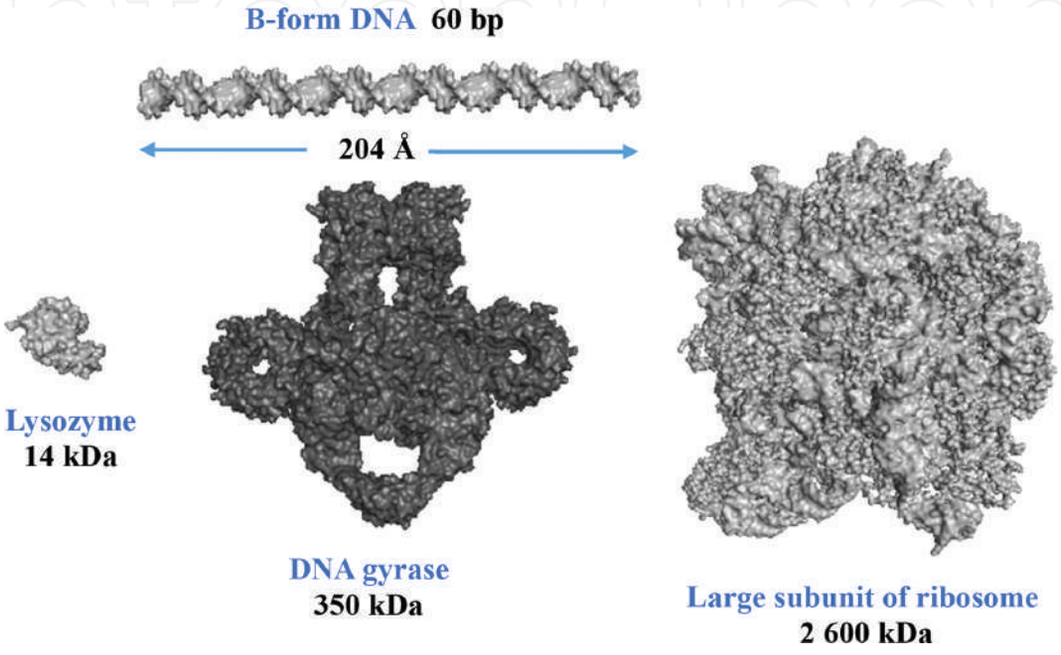

Figure 1. Dimension of biological macromolecules represented at the same scale (picture provided by Dr Jérémie Piton). The length of a 60 base pairs DNA double helix is 204 Å.

Why using X-rays? Their wavelength is of the order of the angström and thus corresponds to the distance between two bound atoms. **Why using a crystal**? To date, the conception of an X-ray microscope encounters two obstacles. First, the signal from a single macromolecule is too low, second, a device, such as lenses, generating a direct image of a macromolecules, does not exist for X-rays. Using a crystal, that contains about 10^{15} identical macromolecules periodically arranged in the three directions of space, overcomes these obstacles.

In only 50 years, crystallography has become the technique of choice for the determination of structures of biological macromolecules at atomic scale, taking advantage of the major advances in the scientific fields as diverse as molecular biology, biochemistry, computer science, physics and more recently robotics. Today, crystallography is able to address the determination of three-dimensional structures of macromolecules more and more complex, more and more quickly. Currently, more than 25 crystal structures are deposited daily in the Protein Data Bank (http://www.rcsb.org)[1] [5].

[1] The protein Data Bank (PDB) is a databank that contains 120,262 entries of macromolecules structures (protein, nucleic acids, complexes), 107,455 have been solved by X-ray crystallography (July 2016).

http://dx.doi.org/10.5772/64999

The physical principle of crystallography is based on X-ray diffraction by all the electrons constituting the atoms of all the macromolecules contained in the crystal (**Figure 2**). The analysis of these diffraction data then allows the crystallographer to calculate the electron density, which is the distribution of the electron cloud of the macromolecule in the crystal. This electron density provided it is sufficiently precise—this preciseness depends on the resolution of the diffraction data—allows the localization of each atom of the molecule, and thus the determination of its coordinates in the three-dimensional space [6].

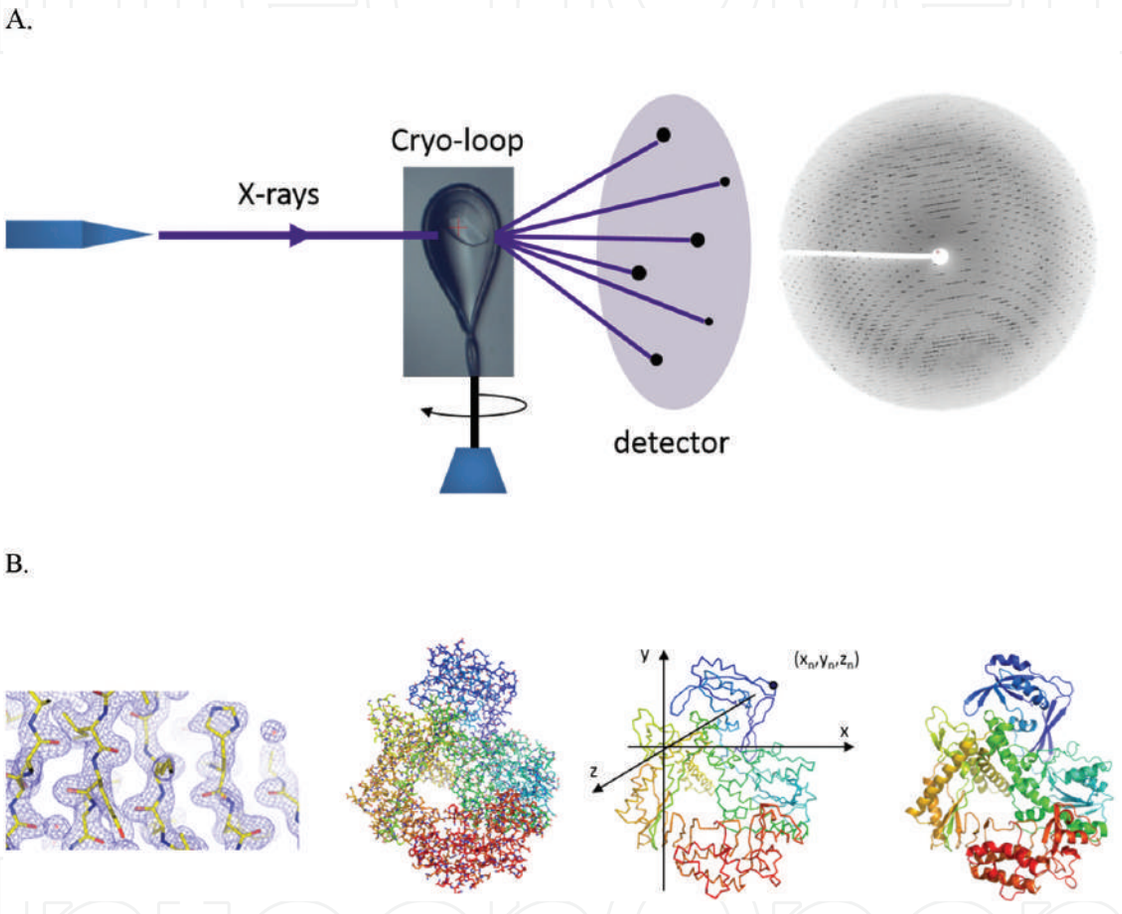

Figure 2. The principle of crystallography. (A) A monochromatic X-ray beam bombards a crystal frozen in a cryo-loop that rotates on itself. The observed diffraction spots are the result of the impact on the detector of the wave diffracted by the electrons in the crystal. (B) Electron density map of a fragment of a macromolecule is represented (left). The three-dimensional structure of a macromolecule (here a protein) is represented in three ways: all-atoms, backbone and cartoon representation (see **Figure 9**).

To get this three-dimensional structure, several steps that falls within multiple disciplines are required (**Figure 3**). Each of these steps represents potential bottlenecks that need to be overcome. These are the production and the purification of the macromolecule, its crystallization, diffraction data collection and processing. Another crucial step is the determination of the phases of the measured signal, absolutely required to calculate the electron density. The last step is the refinement of the built structure, called the model, which will then be interpreted in the context of its biological function. The analysis of the model will thus raise new questions

leading to the resolution of other crystal structures, such as structure of a complex between the studied protein and its partners [7]. We will in the following sections describe each of these steps.

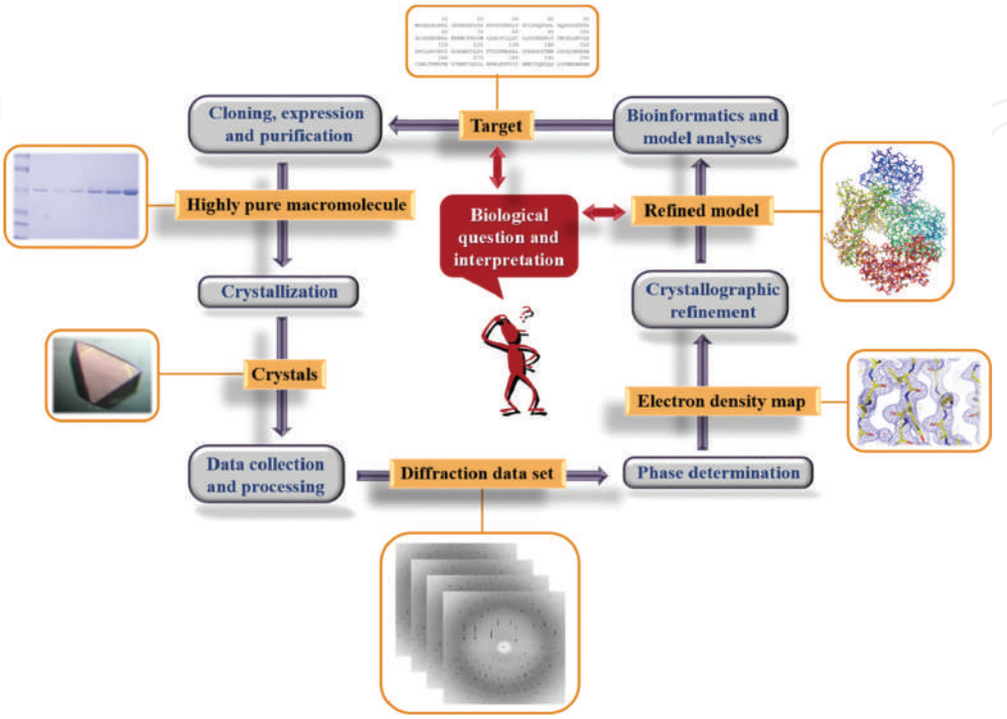

Figure 3. The main steps of the three-dimensional structure determination of biological macromolecules by crystallography.

2. Steps upstream the structure determination

The first step, a step that falls within biology and includes molecular biology and biochemistry techniques, is the production of highly pure macromolecule in large quantity. Once the sequence of the macromolecule to be studied has been identified and characterized by bioinformatics analyses, the sequence corresponding to the gene of the macromolecule is cloned in an expression vector and produced classically in a bacterial organism (typically *Escherichia coli*). The macromolecule is then extracted from the bacterial cells and purified using chromatographic techniques. The prerequisite for the next step is to obtain a concentrated[2] (of the order of tens of grams per liter) and highly pure sample (greater than 98%) of the macromolecule.

The next bottleneck is based on physical chemistry, specifically crystallization which addresses concepts such as solubility of molecules and their transition from soluble state to a solid

[2] In a aqueous solution containing a buffer, salt and various additives.

http://dx.doi.org/10.5772/64999

crystalline ordered state [8]. This step, built on statistical screenings plays with the variation of parameters such as temperature, pH, concentrations of biological macromolecules, as well as nature and concentration of crystallizing agents and various additives [9]. Obtaining a single homogeneous crystal, that result to high quality diffraction data, represents a crucial step in the process of determining a macromolecular structure. In order to increase the success rate, crystallization robots are used today to screen more than several thousands of parameters. The size (from tens to hundreds of microns) and the morphology of the crystals are highly variable (**Figure 4**) and are not necessarily related to their diffracting power and quality.

Figure 4. Crystals of biological macromolecules. Left, a typical crystallization plate used in crystallization robots that allows to screen 96 crystallization conditions. Middle, different crystals of macromolecule. Right, the crystal is shown in its cryo-loop (see Section 2.). The black bar is 100 microns.

3. The diffraction data

The crystals obtained during the previous step are fished using a small loop (**Figure 4**), cryo-cooled to protect them from radiation damage [10], and then placed into a monochromatic X-ray beam produced by an appropriate source, either a rotating anode generator available in crystallography laboratories or a synchrotron radiation, the latter producing significantly more intense beams [11]. Under these conditions, the waves scattered by the electrons of the macromolecules that are three-dimensionally ordered in the crystal add up in given directions (the diffracted beam is characterized by a structure factor, **Figure 7**) and generate a diffraction spot on the screen of the detector (**Figure 5A**). All the spots, regularly spaced, form the diffraction pattern (**Figure 5A**). This diffraction pattern is reconstituted by using several hundreds of images, each corresponding to an orientation of the crystal that rotates on itself during the measurement of the diffraction data (**Figure 2** and **Figure 5B**). The information contained in each diffraction spot is characterized by the amplitude and the phase of the structure factor characterizing the corresponding scattered wave.

The three-dimensional distribution of the spots is directly related to the cell parameters, e.g. the three lengths of the parallelepiped that constitutes the volume element (the cell), which is regularly repeated in space (**Figure 6**) and allows to describe the crystal. The distribution of the spot intensities is directly related to the electron density distribution (the macromolecules) in the cell. Mathematically, this means that the diffraction pattern is the Fourier transform of the electron density (**Figure 7**).

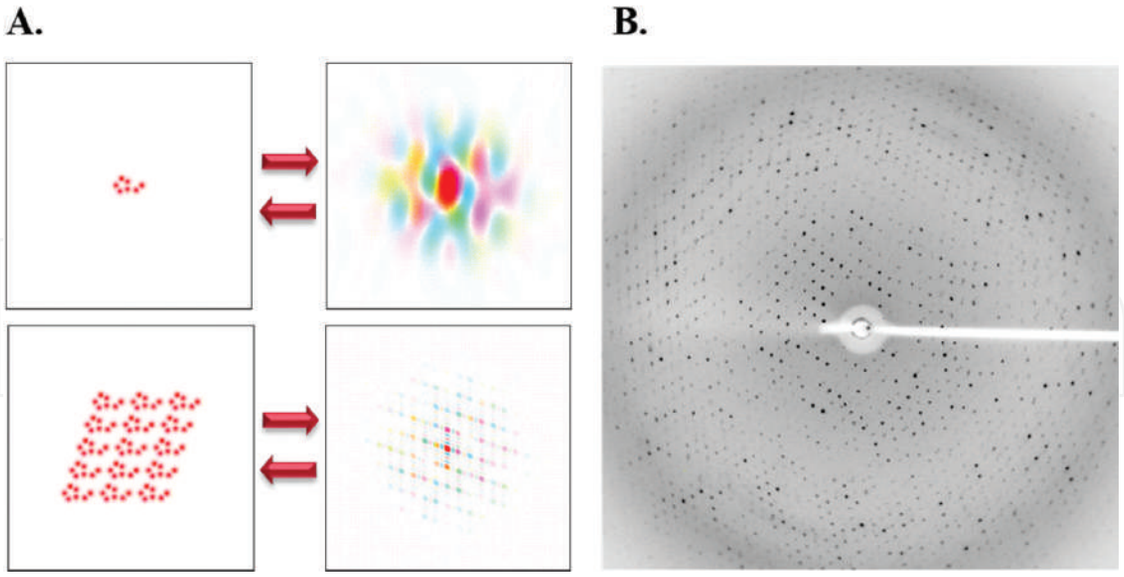

Figure 5. (A) The diffraction pattern (or Fourier transform) of a crystallized molecule generates a three-dimensional spot lattice (bottom), whose background image corresponds to the Fourier transform of a single molecule (top). The amplitude and phase of the diffracted beams are represented by the color brightness and the color hue, respectively (Kevin Cowtan's Picture Book of Fourier Transforms (http://www.ysbl.york.ac.uk/~cowtan/fourier/fourier.html). (B) Example of detector image constituting the diffraction pattern. Hundreds of images are usually recorded. The spots at the image edge are high resolution spots, providing the most detailed information.

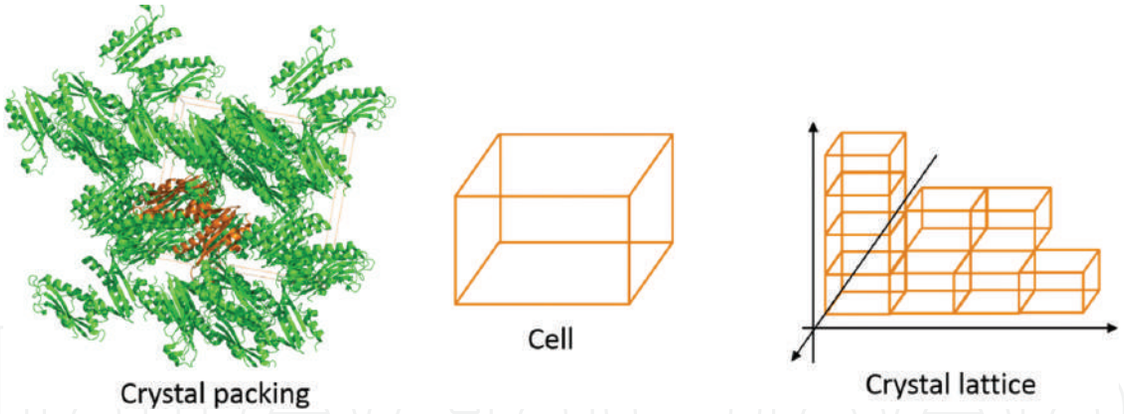

Figure 6. The macromolecules are ordered in the three directions of space and form the crystal packing (left). The smallest volume that is repeated by translation in all directions of space is the cell (middle and right). It forms a parallelepiped characterized by three vectors named a, b and c.

The electron density contained in one cell can thus be calculated by inverse Fourier transform, a mathematical property of this transformation, provided the amplitude and the phase of all the diffracted beams are known (**Figure 7**). Whereas the amplitude is directly proportional to the intensity of the diffracted spots, the phase information is not experimentally measurable.

In summary, the crystal "realizes" a Fourier analysis producing diffraction data, and the crystallographer will calculate a Fourier synthesis to get the electron density contained in one cell (**Figure 7**).

http://dx.doi.org/10.5772/64999

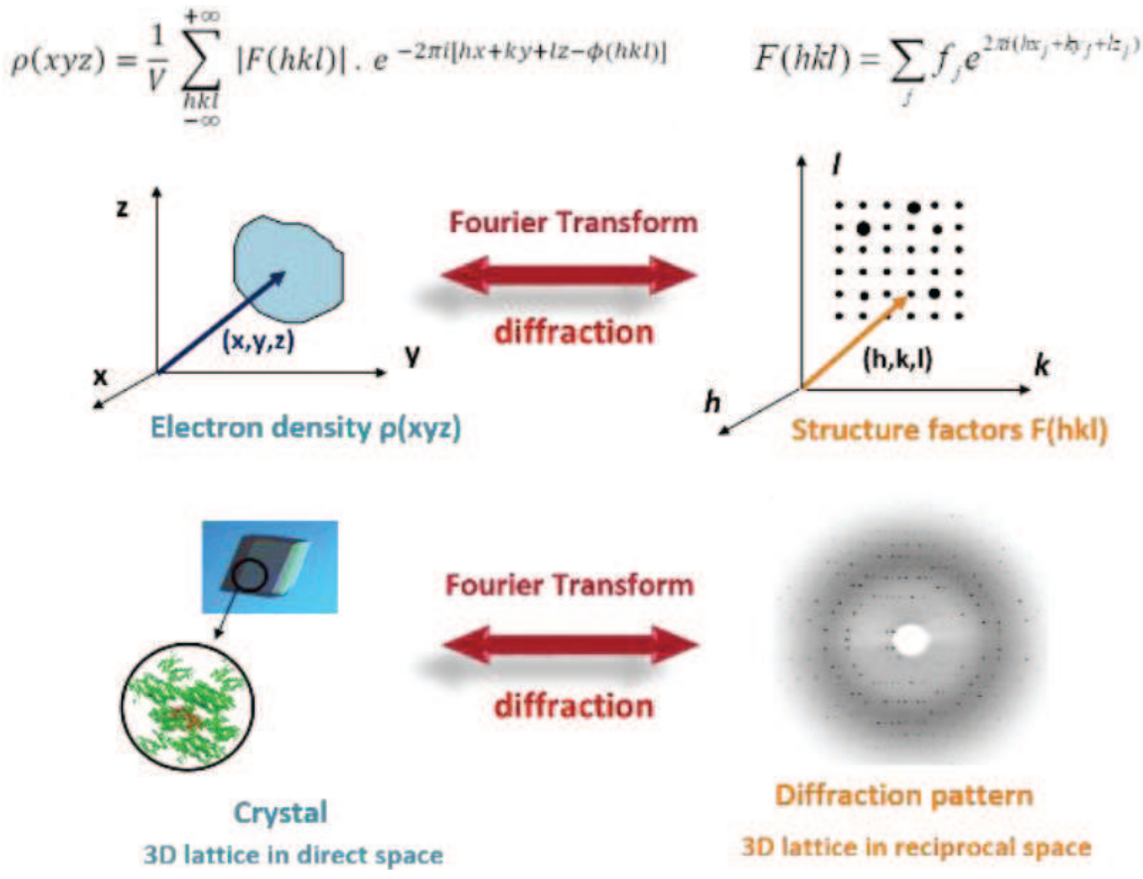

Figure 7. Schematic summary of the relationship between the diffraction (structure factors and diffraction spots) and the electron density of the structure three-dimensionally packed in the crystal.

4. From the diffraction data to the electron density

Three main methods exist for the estimation of the phases [12]. We have to remember here that the number of phases to be estimated is typically several tens to hundreds of thousands (the phase of each spot for which the intensity has been measured has to be estimated).

The first method is *molecular replacement*. It uses the known structure of a homologous protein. To date, approximately 60% of the structures found in the PDB were solved by this method [5]. It consists of constructing a virtual crystal by placing the homologous structure in the cell of the crystal studied using mathematical translation and rotation functions and comparing the diffraction pattern calculated from this virtual crystal and the measured diffraction data. Since the Fourier transforms of two homologous molecules placed in the same crystal are similar, the calculated phases are an excellent approximation of the phases of the measured signal [13–15].

The second method is *multiple isomorphous replacement*, which consists in diffusing heavy atoms (electron-rich) in the crystal [16]. In the first protein structure determination, the phase problem was solved using this method, those of the myoglobin and the hemoglobin [17, 18], by John

Kendrew and Max Perutz in 1960. The presence of the heavy element slightly modifies the diffraction intensities and the comparison of the diffraction pattern in the presence and absence of these heavy elements allows the estimation of the phases by triangulation, after having positioned the heavy atoms in the crystal lattice using methods known as Patterson functions [19].

The third method is *anomalous dispersion*, a specific property of the diffraction pattern when absorption of X-radiation is no longer negligible [20, 21]. This method consists in varying the incident beam wavelength around the absorption edge of one of the atom type contained in the molecule. Comparing the diffraction pattern at different wavelengths will allow the estimation of the phases using methods similar to that of the isomorphous replacement [22]. Selenium is often used because it has an absorption edge near to the wavelengths used (e.g. 1 Å). For proteins, selenomethionine, an amino acid for which the sulfur is replaced by selenium, is generally introduced biosynthetically [23]. In the case of nucleic acids, modified bases containing bromine are frequently used [24].

5. From the electron density to the structural model

Once a first set of phases is estimated, a first electron density map is calculated. If this map is sufficiently interpretable, the macromolecule can be built step by step in this map (**Figure 8**). A combination of automated algorithm and manual method available through interactive graphics softwares are used [25], leading to a final model composed of the three-dimensional coordinates of each atom of the cell content constituted by one or several macromolecules.

From that first built model, the diffraction intensities are calculated by Fourier transform and compared to the intensities experimentally measured. This comparison allows the step by step improvement of the model. This cyclical process is called the crystallographic refinement, alternating the search for global minimum of energy functions and manual reconstruction of the model [26].

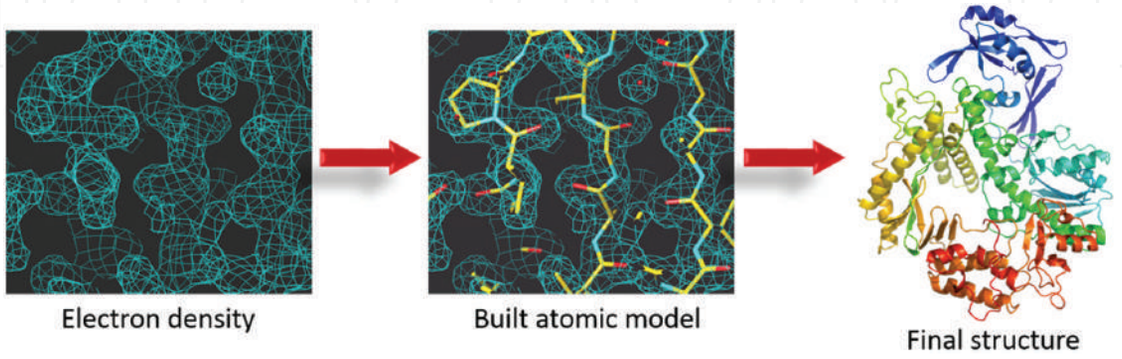

Figure 8. The calculation of the electron density map (left) allows the building of the atomic model step by step (middle) and leads to the three-dimensional model of the structure (right).

http://dx.doi.org/10.5772/64999

6. Steps downstream the structure determination

The final step, downstream the structure determination by X-ray diffraction, concerns the interpretation of the structure and its integration into the biological context [27–29]. It consists in the understanding of the structural result as a three-dimensional object and the appreciation of its function at the cellular or evolution level. The description of the interatomic interactions, the secondary structures (**Figure 9**), the domains and their arrangement that defines the fold or the tertiary structure (**Figure 9**), as well as the characterization of the shape, the electrostatic properties and the quaternary structure based on the content of the cell in the crystal packing, are often complemented by the study of the macromolecule in solution, to better characterize its oligomeric (**Figure 9**) and its dynamic behavior, alone or in the presence of interactors, if known. These studies use a variety of biophysical methods, such as mass spectrometry, analytical ultracentrifugation, light scattering, microcalorimetry or surface plasmon resonance

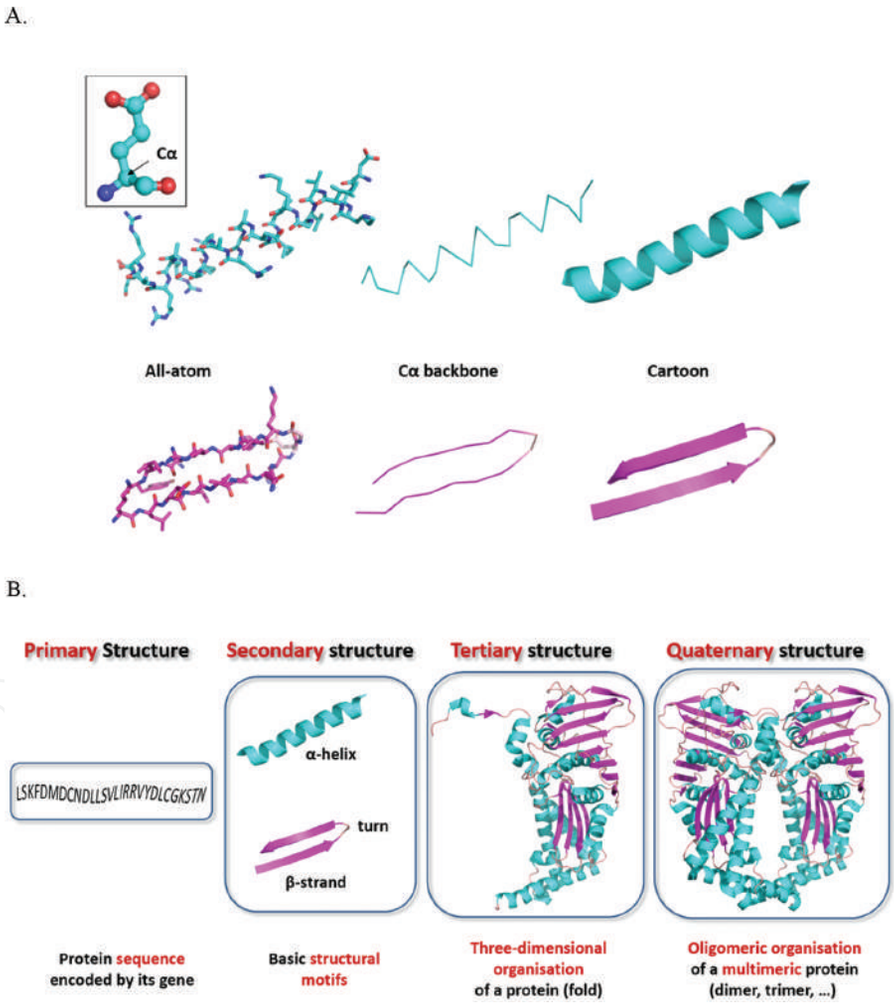

Figure 9. (A) The protein structures are represented by three modes of representation (see also **Figure 2**). The "all-atom" representation shows all the atoms in the protein, the representation "Cα backbone" shows only one atom of each amino acid, the Cα carbon atom, and cartoon representation shows the secondary structures in the shape of a helix for α-helices and in the form of arrows for β-strands. (B) Protein structures are described in four levels, from primary to quaternary structure.

(Biacore® technology), etc … [30]. In the case of enzymes, these studies will be coupled with enzymological approaches to determine the activity and the catalytic constants.

An analysis based on bioinformatics tools will allow to place the structure determined in the context of structural and evolutionary knowledge at a given time [31]. The lessons learned from these studies, often of primary importance, provide information including the classification of the structure and its sequence within a family counterparts, on the distribution and evolution of folding in the different domains of life (viruses, bacteria, archaea, eukaryotes), on the possible function when it is unknown, on the catalytic site and its spatial conservation and sequence, on the degree of oligomerization or on the existence of interaction with other partners, proteins, nucleic acids or ligands. A final type of study seeks to place the three-dimensional object into the context of the knowledge on the major biological mechanisms of live, such as knowledge on gene expression with transcriptomics, on complex formation with interactomics, etc … This information will include the characterization of the partners of the studied macromolecule at the scale of the cell or the whole organism.

All these steps, from the structure determination to the biological interpretation, far from being the end of the story, are often the beginnings of new structural studies (**Figure 3**). These can be articulated around analyses of the relative importance of the components of the macromolecule, the aminoacids, by determining the structure of mutants, or the studies of the interactions with partners by determining the structure of macromolecular complexes.

Author details

Claudine Mayer[1,2,3*]

Address all correspondence to: mayer@pasteur.fr

1 Department of Structural Biology and Chemistry – Institut Pasteur, Paris, France

2 CNRS UMR 3528, Paris, France

3 Paris Diderot University, Sorbonne Paris Cité, Paris, France

References

[1] Watson J.D., Crick F.H.C., Molecular structure of nucleic acids: a structure for deoxyribose nucleic acid. Nature, 1953, 171, p. 737-738.

[2] Anfinsen C., The formation and stabilization of protein structure. Biochem. J., 1972, 128, p. 737–749.

[3] Scapin G., Structural biology and drug discovery. Curr. Pharm. Des., 2006, 12, p. 2087–2097.

[4] Blundell T.L., Johnson L.N., Protein Crystallography. Academic Press, New York, 1976.

[5] Berman H.M., Westbrook J., Feng Z., Gilliland G., Bhat T.N., Weissig H., Shindyalov I.N., Bourne P.E., The Protein Data Bank. Nucl. Acids Res., 2000, 28, p. 235-242.

[6] Wlodawer A., Minor W., Dauter Z., Jaskolski M., Protein crystallography for non-crystallographers, or how to get the best (but not more) from published macromolecular structures. FEBS J., 2008, 275, p. 1-21. Review.

[7] Wlodawer A., Minor W., Dauter Z., Jaskolski M., Protein crystallography for aspiring crystallographers or how to avoid pitfalls and traps in macromolecular structure determination. FEBS J., 2013, 280, p. 5705–5736. Review.

[8] Chernov A.A. Protein crystals and their growth. J. Struct. Biol., 2003, 142, p. 3–21.

[9] Luft J.R., Collins R.J., Fehrman N.A., Lauricella A.M., Veatch C.K., DeTitta G.T. A deliberate approach to screening for initial crystallization conditions of biological macromolecules. J. Struct. Biol., 2003, 142, p. 170-179.

[10] Garman E.F., Schneider T.R. Macromolecular cryocrystallography. J. Appl. Crystallogr., 1997, 30, p. 211-237.

[11] Moffat K, Ren Z., Synchrotron radiation applications to macromolecular crystallography. Curr. Opin. Struct. Biol., 1997, 7, p. 689–696.

[12] Taylor G., The phase problem. Acta crystallogr. D., 2003, 59, p. 1881-1890.

[13] Rossmann M.G. The molecular replacement method. Acta Crystallogr. A., 1990, 46, p. 73-82.

[14] Tickle I.J., Driessen H.P., Molecular replacement using known structural information. Methods Mol. Biol., 1996, 56, p. 173-203. Review.

[15] Abergel C., Molecular replacement: tricks and treats. Acta Crystallogr. D Biol. Crystallogr., 2013, 69, p. 2167-2173. Review.

[16] Perutz, M.F., Isomorphous replacement and phase determination in non-centrosymmetric space groups. Acta Cryst. 1956, 9, p. 867–873.

[17] Perutz M. F., Rossmann M. G., Cullis A. F., Muirhead H., Will G., North A. C., Structure of hemoglobin: a three-dimensional Fourier synthesis at 5.5 A resolution, therefore obtained by X-ray analysis. Nature, 1960, 185, p. 416-422.

[18] Kendrew J.C., Bodo G., Dintzis H.M., Parrish R.G., Wyckoff H., Phillipps D.C., A three-dimensional model of the myoglobin molecule obtained by X-ray analysis. Nature, 1958, 181, p. 662-666.

[19] Patterson A.L., A direct method for the determination of the components of interatomic distances in crystals. Zeitschrift für Kristallographie, 1935, 90, p. 517-542.

[20] Read R.J., As MAD as can be. Structure, 1996, 4, p. 11-14. Review.

[21] Blow D.M., How Bijvoet made the difference: the growing power of anomalous scattering. Methods Enzymol., 2003, 374, p. 3–22.

[22] Ealick S.E., Advances in multiple wavelength anomalous diffraction crystallography. Curr. Opin. Chem. Biol., 2000, 4, p. 495–499.

[23] Doublie S., Preparation of selenomethionyl proteins for phase determination. Methods Enzymol., 1997, 276, p. 523–530.

[24] Anderson A.C., O'Neil R.H., Filman D.J., Frederick C.A., Crystal structure of a brominated RNA helix with four mismatched base pairs: an investigation into RNA conformational variability. Biochemistry, 1999, 38, p. 12577-12585.

[25] Emsley P., Debreczeni J.E., The use of molecular graphics in structure-based drug design. Methods Mol. Biol., 2012, 841, p. 143-159.

[26] Tronrud, D.E., Introduction to macromolecular refinement. Methods in molecular biology series, 2007, vol. 364: macromolecular crystallography protocols: vol. 2: 34 structure determination. p. 231–253, Humana Press Inc, Totowa, NJ.

[27] Baker E.N., Seeing atoms: the rise and rise of crystallography in chemistry and biology, chemistry in New Zealand, January 2011, (New Zealand Institute of Chemistry), New Zealand.

[28] Shi Y., A glimpse of structural biology through X-ray crystallography. Cell, 2014, 159, p. 995-1014.

[29] Yonath A., X-ray crystallography at the heart of life science. Curr. Opin. Struct. Biol., 2011, 21, p. 622–626.

[30] Malik S.S., Shrivastava T., Protein characterization using modern biophysical techniques. Advances in Protein Chemistry, 2013, OMICS Group eBooks. (http://www.esciencecentral.org/ebooks/ebooks-about.php)

[31] Lecompte O., Thompson J.D., Plewniak F., Thierry J., Poch O., Multiple alignment of complete sequences (MACS) in the post-genomic era. Gene, 2001, 270, p. 17. Review.